Eur. Phys. J. D (2013) 67: 200
DOI: 10.1140/epjd/e2013-40153-y

THE EUROPEAN PHYSICAL JOURNAL D

Regular Article

Metastability exchange optical pumping of ^{3}He gas up to hundreds of millibars at 4.7 Tesla

Anna Nikiel-Osuchowska[1,a], Guilhem Collier[1,b], Bartosz Głowacz[1,2], Tadeusz Pałasz[1], Zbigniew Olejniczak[1,3], Władysław P. Węglarz[3], Geneviève Tastevin[2,c], Pierre-Jean Nacher[2], and Tomasz Dohnalik[1]

[1] Marian Smoluchowski Institute of Physics, Jagiellonian University, ul. Reymonta 4, 30-059 Kraków, Poland
[2] Laboratoire Kastler Brossel, ENS, UPMC-Paris 6, CNRS, 24 rue Lhomond, 75231 Paris Cedex 05, France
[3] Institute of Nuclear Physics, Polish Academy of Sciences, Radzikowskiego 152, 31-342 Kraków, Poland

Received 19 March 2013 / Received in final form 26 June 2013
Published online 25 September 2013 –

Abstract. Metastability exchange optical pumping (MEOP) is experimentally investigated in ^{3}He at 4.7 T, at room temperature and for gas pressures ranging from 1 to 267 mbar. The 2^3S-2^3P transition at 1083 nm is used for optical pumping and for detection of the laser-induced orientation of ^{3}He atoms in the rf discharge plasma. The collisional broadening rate is measured (12.0 ± 0.4 MHz mbar^{-1} FHWM) and taken into account for accurate absorption-based measurements of both nuclear polarization in the ground state and atom number density in the metastable 2^3S state. The results lay the ground for a comprehensive assessment of the efficiency of MEOP, by comparison with achievements at lower field (1 mT–2 T) over an extended range of operating conditions. Stronger hyperfine decoupling in the optically pumped 2^3S state is observed to systematically lead to slower build-up of ^{3}He orientation in the ground state, as expected. The nuclear polarizations obtained at 4.7 T still decrease at high pressure but in a less dramatic way than observed at 2 T in the same sealed glass cells. To date, thanks to the linear increase in gas density, they correspond to the highest nuclear magnetizations achieved by MEOP in pure ^{3}He gas. The improved efficiency puts less demanding requirements for compression stages in polarized gas production systems and makes high-field MEOP particularly attractive for magnetic resonance imaging of the lungs, for instance.

1 Introduction

High nuclear polarization can be obtained in ^{3}He gas by metastability exchange optical pumping (MEOP), an indirect but very efficient method to transfer angular momentum from polarized light to the nuclear spins of the atoms [1]. The method involves optical pumping (OP) on the 2^3S-2^3P transition at 1083 nm (a strongly imbalanced distribution of atoms among the hyperfine sublevels is induced in the metastable 2^3S_1 state) and metastability exchange (ME) collisions between metastable and ground state atoms (the nuclear orientation is transferred to the ground 1^1S_0 state). A rf discharge is most often sustained in the gas to retain a small steady-state fraction of the atoms in the 2^3S state. Room temperature MEOP is usually performed in the so-called standard conditions, i.e., at low magnetic field strength (a few milliteslas) where strong hyperfine coupling occurs in the 2^3S state and at low pressure (around one millibar) where pumping is both fast, due to a high enough 2^3S atom relative number density, and efficient, due to moderate plasma-induced angular momentum loss [2]. The low applied magnetic field has a negligible effect on the level structure and only prevents fast magnetic relaxation of the out-of-equilibrium nuclear polarization M prepared by optical pumping ($-1 \leq M \leq 1$). The MEOP-driven polarization exceeds, by many orders of magnitude, the field-induced (Boltzmann) polarization reached at thermal equilibrium. In the ^{3}He gas at 4.7 T and room temperature this equilibrium polarization is small (1.25×10^{-5}) and always neglected. The Zeeman splittings remain much smaller than the Doppler atomic linewidth and the OP light must be circularly polarized to address selected 2^3S sublevels. Under optimal experimental conditions a nuclear polarization exceeding $|M| = 0.8$ is obtained in the ground state with high photon efficiencies, typically one to two polarized nuclei per absorbed photon [2,3]. The highest polarization can be reached at 0.5 mbar and a strong decrease of MEOP efficiency with increasing operating gas pressure is observed

[a] *Present address:* Institute of Physics, Johannes Gutenberg-Universität Mainz, Staudingerweg 7, 55128 Mainz, Germany.
[b] *Present address:* The University of Sheffield, Royal Hallamshire Hospital, Sheffield, S10 2JF, UK.
[c] e-mail: tastevin@lkb.ens.fr

above 1 mbar [4,5]. In the last decades MEOP has been combined with sophisticated techniques of polarization-preserving compression to produce large quantities of hyperpolarized ^{3}He gas for applications where high magnetization densities are needed [6–8]. Improving the efficiency of MEOP at higher pressure could facilitate this compression by significantly reducing the requirements on the compression ratio and pumping speed for the mechanical devices implemented in ^{3}He gas polarizers. It would alternatively provide direct access to larger magnetization densities for in vivo lung imaging by nuclear magnetic resonance (NMR), since one can simply add a neutral buffer gas to the polarized ^{3}He gas to reach atmospheric pressure and allow inhalation [9].

Following the first demonstrations of improved MEOP efficiency at 0.1 T [4,10,11] and 0.6 T [12], a systematic experimental investigation of processes relevant for MEOP in non standard conditions (high field, high pressure, and/or high laser power) has been undertaken [4,5,13,14] and a thorough study of both ME and OP processes at high field has been carried out [15]. Spectacular improvements of the steady-state nuclear polarization have been reported at 1.5 T for gas pressures ranging from 8 to 67 mbar [5,16], as well as at 32 and 67 mbar for field strengths ranging from 0.45 to 2 T [13]. These improvements may be mostly due to reduced losses of nuclear orientation by relaxation since the operation at high field has a limited negative impact on OP and ME. Indeed, the spectrum of the 2^3S-2^3P transition is deeply modified by the applied field but several resonance lines are suitable for OP and, for instance, the measured photon efficiencies are as high at 1.5 T as at low field [16]. In spite of the strong hyperfine decoupling that occurs in the 2^3S state at high field, the transfer of nuclear orientation by ME also remains efficient because the smaller fraction of nuclear orientation transferred by each ME event is compensated by the higher frequency of ME collisions in this pressure range. The pumping time is nevertheless observed to become longer when the gas density is increased, which may be prohibitive for most applications in spite of the gain in magnetization. Still, there may be room for global improvement of MEOP efficiency at fixed gas pressure, by optimization of the experimental conditions such as cell geometry and discharge electrodes [5,13,16] or pump laser characteristics [17] for instance.

The strong increase of nuclear polarization and magnetization with the applied magnetic field strength, up to 2 T, reported in reference [13], has motivated further studies of ^{3}He MEOP, at higher magnetic field and at higher gas pressure in particular. In this article an experimental investigation of MEOP at 4.7 T is reported, with measurements performed both in the two sealed glass cells that had been used in reference [13] (32 and 67 mbar) and in a series of cells with an identical geometry filled with different ^{3}He gas pressures (ranging from 1.33 to 267 mbar). A detailed analysis of the plasma conditions and of the optical pumping results obtained at 4.7 T is presented. The reported work is a milestone in the systematic investigation of MEOP in that it concludes a series of pioneering studies at high field and high laser power. This article, therefore, includes a comparison of achievements at 4.7 T and at lower field strengths, for a global assessment of the efficiency of high-field MEOP and a prospective optimization of the operating conditions. It also includes qualitative or quantitative elements of information omitted in the previous reports and it provides a state-of-the art description of the optical method used for accurate measurements of ^{3}He nuclear polarization at high field. This comprehensive report is intended to lay the ground for further in-depth studies of MEOP and to provide useful tools for a rapid development of new high-field applications.

Experiment and methodology are described in Section 2, where OP and detection techniques are presented with emphasis on the features that are specific to operation at high field and at high gas pressures. The experimental arrangement, OP scheme, and measurement protocol are similar to those used in the 0.45−2 T study [13,18]. They are briefly described in Sections 2.1 to 2.3. The absorption-based technique used to measure the ^{3}He nuclear polarization and to monitor its time evolution, valid at all field strengths [15], involves a weak excitation of the 2^3S-2^3P transition at 1083 nm. Its implementation at high field has been briefly presented in references [18,19]. However, the operation at high gas pressure makes data reduction substantially less straightforward than in the previous studies at low (1.33 mbar [5]) and moderate (8 to 67 mbar [5,13]) pressure, due to strong collisional broadening and overlap of the probed resonance lines. The method developed for the analysis of the light absorption signals is described in Section 2.4, where the 2^3S-2^3P collisional broadening rate is measured and taken into account for accurate measurements of both nuclear polarization in the ground state and atom number density in the metastable state. Then, Section 2.5 introduces the parameters used to fully describe MEOP dynamics at 4.7 T and to quantitatively assess its efficiency in view of applications.

The experimental results are presented in Section 3. The report includes a detailed analysis of the plasma conditions met in each cell at 4.7 T (Sect. 3.1) and of their impact on MEOP dynamics (Sect. 3.2), then of the influence of the incident pump light power at fixed plasma conditions (Sect. 3.3). Finally, the implications for practical implementation of high-field MEOP and optimization of this powerful method are discussed (Sect. 3.4). The discussion is based on a global compilation of the 4.7 T data and on a comparison between these results and those obtained at lower field in the same OP cells, which includes both the 32 and 67 mbar data published in reference [13] and a new series of 32–267 mbar data (reported here) from a complementary investigation performed at 2 T[1]. Prospects of high field operation are briefly considered for MEOP-based production of polarized gas, having in mind the use of ^{3}He in neutron spin filters and in MRI.

Color (available on line) is used in some figures, only to provide a further guide to the eye.

[1] Unpublished Ph.D. work by the first author (A.N.-S.) [20].

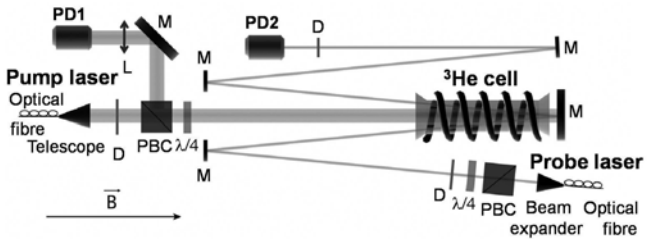

Fig. 1. Optical apparatus used for MEOP at 4.7 T (not to scale). Thick (resp. thin) straight lines: optical path of the pump (resp. probe) beam. A $f = 8$ mm lens collimator and a 7-fold magnifying Kepler telescope are used to expand the OP beam. Labeled components: polarizing beam splitter cubes (PBC), quarter-wave plates ($\lambda/4$), photodiodes (PD1 and 2), mirrors (M), a collecting lens (L) for the OP beam, and circular diaphragms (D). The pump (resp. probe) beam diameter is about 15 (resp. 1.5) mm.

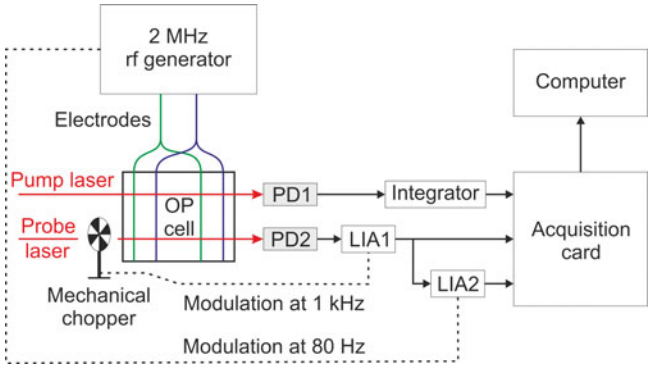

Fig. 2. Block diagram of the data acquisition scheme. PD1, PD2: photodiodes. LIA1 (resp. 2): lock-in amplifier for fast (resp. slow) demodulation of the transmitted probe light signal delivered by PD2. A rf amplifier and a tuned transformer (not shown) are also used to obtain the high voltage applied to the external wire electrodes.

2 Experiment and methodology

2.1 Setup

Experiments are performed in a Bruker 4.7 T superconducting magnet routinely used for animal MRI studies. The setup is very similar to that used for the investigation of MEOP up to 2 T [13]. The non-magnetic optical components depicted in Figure 1 are mounted on an aluminum breadboard inside the 30 cm diameter horizontal bore of the magnet.

Five sealed cells filled at room temperature with pure ^{3}He gas at pressures roughly equal to 32, 67, 96, 128, and 267 mbar are used. Additional tests are performed in a 1.33 mbar cell. Each homemade cell consists in a Pyrex tube (15 mm inner diameter, 1.5 mm wall thickness) closed at both ends by a flat Pyrex window (30 mm diameter, 2 mm thickness). The larger diameter of the end windows that gives the cell the "bone-shaped" profile sketched in Figure 1 avoids major beam distortion in the central part, potentially allowing a full coverage of the inner cross section of the tube by the wide OP beam. All cells have approximately the same internal length ($L_{\rm cell} \simeq 12$ cm) and inner volume ($V_{\rm cell} \simeq 20$ cm^3). A high voltage is applied at 2 MHz to two interleaved spiral electrodes wired on the outer surface of the tube to generate a weak rf discharge (same winding orientations, pitches comparable to the cell diameter).

The optical apparatus includes two main parts, the optical pumping and the detection systems. A broadband (1.7 GHz FWHM) ytterbium fiber laser with 10 W maximum output power (Keopsys, type CT-YFL-1083-He-100) is used for OP. The light exiting the polarization maintaining single-mode output fiber is collimated and expanded into a 4.9 mm FWHM Gaussian beam. This beam is circularly polarized and diaphragmed before entering the helium cell. A double-pass scheme is implemented to increase the absorption of the OP light by the atoms. This advantageously provides a simple way to measure the absorbed light power using a collecting lens and a photodiode (PD1 in Fig. 1), since the back-reflected pump beam transmitted through the quarter-wave plate is deflected at 90° from the propagation axis by the polarizing beam splitter cube. A single-frequency DBR laser diode emitting at 1083 nm (SDL 6702-H) is used to probe the 2^3S atom density and to measure the ^{3}He nuclear polarization with the absorption method described in Section 2.4.3. The diode output beam is injected into an optical fiber, then collimated, expanded, circularly polarized, and diaphragmed to obtain a narrow probe beam with uniform power density, weak enough ($\sim$100 μW cm^{-2}) to avoid artifacts caused by saturation or OP effects [15,19]. The emission frequency is adjusted by temperature control of the laser diode. It is linearly swept up and down, through two weak resonance lines in the ^{3}He absorption spectrum, to alternatively probe two sublevels of the 2^3S state not addressed by the pump light (see Sect. 2.2 and Fig. 3).

In contrast with reference [13], where a similar longitudinal probe bream configuration was used, a double modulation scheme is implemented for the probe acquisition channel (Fig. 2). As usual, to improve sensitivity for the polarization measurements and to separate the contribution of the resonant atomic response from that of the infrared stray light background in the PD2 photodiode signal, the amplitude of the rf voltage applied to the electrodes is slightly modulated at 80 Hz (15% modulation depth). This induces a synchronous variation of the number density $n_{\rm m}$ of 2^3S atoms in the plasma[2], hence of the optical thickness. The corresponding change in transmitted probe light power is analyzed using a digital lock-in amplifier (Stanford Research Systems SR830, "LIA2" in Fig. 2). The probe beam propagates almost collinearly with the pump beam (see Fig. 1). To remove any spurious

[2] The modulation period should optimally be long compared to the 2^3S atom lifetime to avoid damping of the rf-driven oscillation. The upper bounds set by diffusion to the walls (0.2−35.4 ms, proportional to pressure [21]) are 1 or 2 orders of magnitude larger than the lifetimes measured in the OP cells above 32 mbar, due to conversion to metastable He dimers [22].

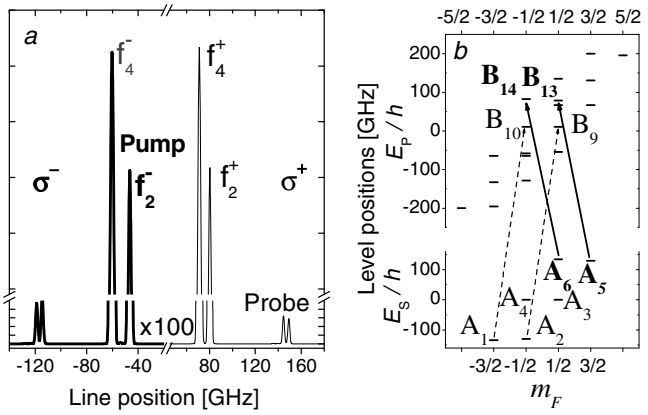

Fig. 3. Hfs of the 2^3S-2^3P transition at 4.7 T [15]. (a) Absorption spectra computed at 300 K (no pressure broadening). Left, thick line: σ^-; right, thin line: σ^+; horiz. axis: frequency shifts from C_1 line at 0 T. The strong f_2^- line labeled "pump" is used for OP, the weak lines of the σ^+ doublet labeled "probe" for detection. (b) Energy diagram of 2^3S and 2^3P states (vert. axes: E_S, resp. E_P, in frequency units; ref.: 2^3P_2 energy at 0 T). The pump (resp. probe) laser simultaneously (resp. sequentially) addresses the sublevels connected by the solid (resp. dashed) arrows.

contribution from the transmitted pump light[3] to the PD2 photodiode signal, a mechanical chopper (inserted on the probe beam path before injection into the fiber) additionally modulates the incident probe power at about 1 kHz. A lock-in amplifier ("LIA1" in Fig. 2, identical to the other one but operating at this higher reference frequency) performs an initial fast demodulation of PD2 output voltage and feeds in the second lock-in amplifier, LIA2.

Three analog signals are recorded using a data logger (National Instruments, type 6221) interfaced to a personal computer via its PCI port and subsequently processed offline to obtain: (1) the average transmitted pump power, provided by the integrator that filters out the 80 Hz modulation in PD1 output voltage; (2) the average transmitted probe power, provided by numerical time integration of LIA1 output voltage; (3) the amplitude of the (plasma-induced) modulation of the transmitted probe power, provided by LIA2; (4) the modulation depth of the probe signal, from the ratio of item 3 to item 2. In-house compiled programs and a scientific graphing software (OriginLab) are used for data reduction and analysis.

2.2 Optical pumping and detection schemes

Figure 3 shows the 1083 nm absorption spectrum of ^{3}He for circularly polarized light and the energy diagram of the 2^3S and 2^3P states, numerically computed at 4.7 T with the hyperfine structure (hfs) provided in reference [15]. The 2^3S (resp. 2^3P) magnetic sublevels are labeled A_i (resp. B_j), by increasing values of the energy

[3] Its modulation in power is also due to that of n_m. Lock-in amplification of PD1 signal (not performed here) would give access to relative changes in pump absorption (see Sect. 2.4).

Table 1. A_i, $B_j(\infty)$: asymptotic quantum states for $B = \infty$. $T_{ij} = |\langle A_i|T(\sigma^\pm)|B_j\rangle|^2$: transition matrix element, with $\langle m_S : m_I|T(\sigma^\pm)|m_L,\ m'_S : m'_I\rangle = \delta(m_L,\ \pm1) \times \delta(m_S,\ m'_S) \times \delta(m_I,\ m'_I)$. Line position unit: GHz. The probe lines (top rows) are separated by 4.6 GHz. The f_2^- line (bottom row) has two components with 0.4 GHz hyperfine splitting.

	$A_i(\infty)$	$B_j(\infty)$	T_{ij}	Position
A_1-B_{10}	$\mid -1\colon -1/2\ \rangle$	$\lvert 0, 0 : -1/2\rangle$	0.01748	149.147
A_2-B_9	$\mid -1\colon 1/2\ \rangle$	$\lvert 0, 0 : 1/2\rangle$	0.01935	144.540
A_5-B_{13}	$\mid 1\colon 1/2\ \rangle$	$\lvert -1, 1 : 1/2\rangle$	0.9471	–46.356
A_6-B_{14}	$\mid 1\colon -1/2\ \rangle$	$\lvert -1, 1 : -1/2\rangle$	0.9688	–46.789

E_S (resp. E_P). Hyperfine decoupling is strong: the eigenstate has a single leading component $|m_S : m_I\rangle$ (resp. $|m_L, m_S : m_I\rangle$ in the (L, S, I) representation) and the energy shift is dominated by the linear Zeeman contribution of the magnetic field B, $(g'_L m_L + g'_S m_S + g'_I m_I)\mu_B B$.[4] The energy diagram, therefore, includes pairs of nearly degenerate sublevels with identical electronic quantum number(s) and $m_I = \pm 1/2$ (hyperfine splitting: 33 MHz/T), distributed in a symmetrical equally-spaced pattern (fine splitting: 28, resp. 14 GHz/T).

The graph in Figure 3a only displays the main lines of the σ^+ and σ^- Doppler broadened absorption spectra. For both, the selected frequency range includes the 8 components that have relative weights exceeding 1% (note the broken horizontal axis). The full spectrum includes 22 hyperfine components for each polarization, with line centers distributed between −257.5 and +269.4 GHz around the position of the C_1 line at $B = 0$ ($2^3S_1, F = 1/2$–$2^3P_2, F = 3/2$). Following references [5,13,23], the strong lines are labeled f_2 and f_4 (depending on the number of unresolved hyperfine components) with superscripts ± standing for $\sigma^\pm$ light polarizations.

The present study focuses on experiments performed with the OP and detection scheme sketched in Figure 3b. It is similar to the scheme used at 1.5 T [23] and 2 T [13,18] and involves the transitions described in Table 1. The broadband pump laser is tuned to the strong f_2^- line that also yields the highest nuclear polarization at 4.7 T. This two-component line (shown by the solid arrows in Fig. 3b) addresses the highest-energy 2^3S sublevels, A_5 and A_6. The monochromatic probe laser is tuned to a roughly 190 GHz higher frequency and it alternatively scans the two single-component lines (dashed arrows in Fig. 3b) that belong to the weak σ^+ doublet labeled "probe" in Figure 3a (note the change in vertical scales). This is used for measurement or comparison of the atomic populations in the lowest-energy 2^3S sublevels, A_1 and A_2, that are not excited by the pump laser. For both lasers the quality of the circular polarization of the light is actually not crucial at 4.7 T because the Zeeman splittings, considerably larger than the laser and atomic linewidths, bring the residual wrong circular component completely out of resonance.

[4] L and S: electronic orbital momentum and spin; I: nuclear spin. Coefficients: g-factors for ^{3}He; μ_B: Bohr magneton; $g'_L = 0$ for 2^3S and $g'_L \simeq 1$ for 2^3P; $g'_S \simeq 2$; $g'_I \simeq 2.3 \times 10^{-3}$ [15].

2.3 Measurement protocols

For each OP cell a full experimental run includes a series of data acquisitions performed at various rf excitation levels (for fixed OP light power) and at various OP light powers (for fixed rf level). Inside the 4.7 T magnet rf discharges are rather difficult to ignite at high gas pressure. Therefore, once a stable discharge with suitable intensity is obtained, ample time is allowed for warming-up of the rf electronics (in particular the voltage transformer) and stabilization of the cell temperature (affected by the deposited rf power). Then, all measurements are performed in a row before the discharge is switched off. The data acquisition time sequence typically includes the recording of the optical signals for a few probe scans performed at null polarization with the OP beam blocked, then during polarization build-up with the OP beam on, and finally during polarization decay with the OP beam blocked again. The main difference with the standard protocol used for low-field MEOP studies is that the rf discharge is never turned off during the recording of MEOP dynamics. This preserves the stability of the plasma but does not allow for, e.g., absolute measurements of the absorbed pump and probe light powers at steady-state polarization [24].

Due to strict time constraints (a 4-week period of access time to the 4.7 T MRI magnet granted for the whole study), the experimental runs are planned to include investigations for a combination of three discharge intensities and three pump power conditions, with limited opportunities for tests of reproducibility. Preliminary tests of 1083 nm light absorption are performed with the probe and a weak OP beam to select the rf levels for which OP dynamics will be compared. For these levels, static absorption measurements are performed to obtain absolute values of the 2^3S atom density at null polarization. Then, at fixed OP light power (0.5 W), the three full OP dynamics (build-up and decay) are successively recorded. For the last and strongest discharge, two additional recordings of the polarization build-up are performed at higher power (1 and 2 W) before the discharge is switched off. The data at 0.5, 1, and 2 W are thus acquired in identical plasma conditions, which are expected to be fairly close to those characterized by the initial static measurements given the generally good reproducibility of the results.

2.4 2^3S-2^3P light absorption measurements

2.4.1 Probe light absorption by the plasma

Absolute measurements of 2^3S-2^3P light absorption can be performed using the time-integrated component of the probe signal, by comparison of the average light powers $\mathcal{P}_{\rm on}$ and $\mathcal{P}_{\rm off}$ transmitted through the cell with and without rf discharge, respectively. But relative changes in light absorption are more accurately tracked using the demodulated component which, by ratio to the time-averaged component, yields the modulation depth q of the probe signal. This is a robust quantity, insensitive to fluctuations in laser power and, to first order (see Appendix A), proportional to the light absorbance:

$$q \propto -\ln\mathcal{T},$$

where $\mathcal{T} = \mathcal{P}_{\rm on}/\mathcal{P}_{\rm off}$ is the transmittance of the plasma. The global scaling factor introduced by this measurement technique is related to the amplitude of the plasma response to the small modulation of the rf excitation voltage. It is identical for all 2^3S-2^3P lines, hence irrelevant for all the measurements that involve only absorbance ratios.

Optical detection is performed by single-frequency excitation with a weak laser beam that has a small diameter and a uniform intensity. Hence, the plasma absorbance is given by (see Appendix C.1):

$$-\ln\mathcal{T} = L_{\rm path} n_{\rm m}^{\rm s} \sigma(\nu_{\mathcal{L}}, e_+), \tag{1}$$

where $L_{\rm path}$ is the length of the probe beam path in the gas, $n_{\rm m}^{\rm s}$ the 1D spatial average of the 2^3S density along this path (Eq. (15) in Sect. 2.4.4), and σ the cross section for monochromatic light absorption ($\nu_{\mathcal{L}}$ and e_+: probe frequency and polarization vector, respectively).

Spectral amplitudes

Inside the OP cells the optical transition rates are affected by the Doppler and the collisional line broadening processes, which leads to a significant change in atomic line shape (from a Gaussian to a broad Voigt profile) for increasing gas pressure. For simplicity, collisional broadening is assumed to be identical for all 2^3S-2^3P hyperfine components and the small differences in Doppler widths due to Zeeman shifts are neglected. The same Voigt line shape is thus assigned to each resonant contribution to absorption, characterized by a Gaussian FWHM $\overline{\omega}_{\rm G}$ and a Lorentzian FWHM $\overline{\omega}_{\rm L}$. Following reference [15] and using similar notations, for negligible stimulated emission[5] the cross section σ can be written as:

$$\sigma(\nu, e_\lambda) = \sum_{i,j} a_i T_{ij}(e_\lambda)\, \tilde{\sigma} I_{\rm Voigt}(\nu - \nu_{ij}). \tag{2}$$

The sum includes all transitions excited by the incident monochromatic light (frequency: ν, polarization vector: e_λ). The A_i-B_j contribution (resonance frequency: ν_{ij}) involves: a_i, the population of initial sublevel A_i; T_{ij}, the transition matrix element; $\tilde{\sigma}$, the Gaussian normalization coefficient associated with the gas temperature $T_{\rm gas}$:

$$\tilde{\sigma} = \hbar \frac{\sqrt{\pi}\alpha f}{m_e \tilde{\Delta}_3}, \tag{3}$$

where the average Doppler width $\tilde{\Delta}_3$, given by:

$$\tilde{\Delta}_3 = \overline{\omega}_{\rm G}/(2\sqrt{\ln 2}), \tag{4}$$

[5] Equation (2) can be directly extended to the case of strong 2^3S-2^3P excitation by replacement of a_i with $(a_i - b_j)$, where $n_{\rm m} b_j$ is the number density of ^{3}He atoms in sublevel B_j [24].

replaces the exact one, $\Delta_3^{ij} = \nu_{ij}\sqrt{2k_BT_{\rm gas}/M_3c^2}$. $I_{\rm Voigt}$ is a dimensionless Voigt integral defined as:

$$I_{\rm Voigt}\left(\nu-\nu_{ij}\right) = \frac{\sqrt{\ln 2}}{\pi}\frac{\overline{\omega}_{\rm L}}{\overline{\omega}_{\rm G}} \times \int_{-\infty}^{\infty} \frac{\exp(-u^2)\,du}{\left(\sqrt{\ln 2}\overline{\omega}_{\rm L}/\overline{\omega}_{\rm G}\right)^2 + \left(2\sqrt{\ln 2}\left(\nu-\nu_{ij}\right)/\overline{\omega}_{\rm G} - u\right)^2} \quad (5)$$

so that $I_{\rm Voigt}(\nu-\nu_{ij})$ reduces to the usual Gaussian factor $\exp\{-(\nu-\nu_{ij})^2/(\tilde{\Delta}_3)^2\}$ for dominant Doppler broadening ($\overline{\omega}_{\rm L}\to 0$). In the above expressions, f is the oscillator strength of the 2^3S-2^3P transition ($f = 0.5391$ for helium, with a neglected isotopic effect of order 10^{-4} [25]), M_3 is the atomic mass of ^{3}He. The fundamental constants appear with usual notations: $\hbar$, reduced Planck constant; α, fine structure constant; m_e, mass of the electron; k_B, Boltzmann constant; c, speed of light). Using $\tilde{\Delta}_3 = (\Delta_3^{2,9} + \Delta_3^{1,10})/2$ for computation, the cross-section prefactor is given by:

$$1/\tilde{\sigma} = 1.4719\sqrt{T_{\rm gas}^{\rm K}/300}\times 10^{15}\ \text{m}^{-2} \quad (6)$$

and the Gaussian FWHM to:

$$\overline{\omega}_{\rm G} = 1.9784\sqrt{T_{\rm gas}^{\rm K}/300}\ \text{GHz}, \quad (7)$$

where $T_{\rm gas}^{\rm K}$ is the value of $T_{\rm gas}$ in Kelvin.

In equation (2) the coefficient $\tilde{\sigma}$ simply yields a global temperature dependent cross-section prefactor, identical to that obtained for pure Doppler broadening. A dimensionless spectral amplitude S, equal to:

$$S(\nu,e_\lambda) = \sum_{i,j} a_i T_{ij}\left(e_\lambda\right) I_{\rm Voigt}\left(\nu-\nu_{ij}\right), \quad (8)$$

thus fully characterizes the absorption spectrum, whose shape varies both with the distribution of populations in the 2^3S state and with the (relative) importance of collisional broadening. The probe absorbance can then be expressed as:

$$-\ln\mathcal{T} = L_{\rm path} n_{\rm m}^{\rm s}\tilde{\sigma}S(\nu_{\mathcal{L}},e_+) \quad (9)$$

where, for shorter notation in text and figures, $S(\nu,e_+)$ will often be replaced by $S^+(\nu)$ in the following sections.

Equation (9) is used for the analysis of all absorption-based measurements performed with the probe laser beam. This analysis relies on the strong coupling between the 2^3S state populations a_i and the ^{3}He nuclear polarization M which is introduced by the frequent ME collisions (M is defined by the relative populations $(1\pm M)/2$ of the hyperfine sublevels $m_I = \pm 1/2$ of the ground state).

Spin-temperature equilibrium

When ME dominates, a Boltzmann-like distribution of angular momenta is established in the 2^3S state ($a_i \propto e^{\beta m_F}$), fully ruled by M and characterized by an effective spin-temperature parameter $1/\beta$ given by $e^\beta = (1+M)/(1-M)$ [1,15,24]. The spin-temperature equilibrium populations a_i are equal to:

$$(1\pm M)^3/\left(6+2M^2\right) \quad \text{for} \quad m_{\rm F} = \pm -3/2,$$

and

$$(1\pm M)\left(1\mp M^2\right)/\left(6+2M^2\right) \quad \text{for} \quad m_{\rm F} = \pm 1/2.$$

The nuclear polarization M can thus be inferred from two absorption measurements, performed for identical $n_{\rm m}^{\rm s}$, independently probing the distribution of populations a_i. Conversely, measurements performed for known M provide access to the average number density $n_{\rm m}^{\rm s}$.

In practice, absorption is measured at resonance, which provides the largest signal value. If only one component A_i-B_j contributes to light absorption, the spectral amplitude is simply equal to $S^+(\nu_{ij}) = a_i T_{ij} I_{\rm Voigt}(0)$. In this case peak absorbances can be directly compared, without detailed knowledge of the atomic line shape, to infer M from the probed population ratio. The FHWM values are needed only to compute $I_{\rm Voigt}(0)$ for absolute measurements of $n_{\rm m}^{\rm s}$ when $\overline{\omega}_{\rm L}$ is not negligible compared to $\overline{\omega}_{\rm G}$. Otherwise data reduction is not straightforward and, as shown below, spectral amplitudes computed with actual atomic linewidths are required for accurate measurements.

Impact of 2^3S-2^3P collisional broadening

At room temperature the Doppler FWHM is 2.3 times smaller than the doublet splitting. As shown below, the two probe lines remain fairly resolved for small collisional broadening. When $\overline{\omega}_{\rm L}$ increases, the Lorentzian wings of the remote lines (mainly the intense lines f_4^+ and f_2^+) give rise to a slanted baseline for the doublet spectrum. Therefore, the ratio of the peak absorbances systematically differs from a_2/a_1. This difference persists for the baseline-corrected spectrum, because the two probe lines also overlap significantly and each peak value includes combined contributions from atoms in the A_1 and A_2 sublevels.

The change in the line shape is illustrated in Figures 4a and 4b where processed data (q) are displayed for frequency scans performed at low and high gas pressure, respectively. The first four scans are performed at $M = 0$ and without OP. The spectra obtained in the 1.33 mbar cell exhibit a flat baseline and well resolved resonance lines. In the 128 mbar cell, the line doublet is partly resolved and for each scan a significant baseline is observed. Figure 4c displays the corresponding baseline-corrected data (q'). The baselines cannot be reliably computed when OP is performed because of the ill-known population imbalance induced by the intense OP light [5,14,23,24]. Instead, they are corrected for by substraction of linear baselines that are automatically adjusted to the data for the monotonic parts of the alternating frequency sweeps. The adjusted baselines (shown by straight line segments in Fig. 4b) are consistent with the true ones, obtained for the matching computed spectra (see Fig. 5b). The slopes alternate in sign with the frequency sweep direction (up or down) and vary in magnitude when M increases.

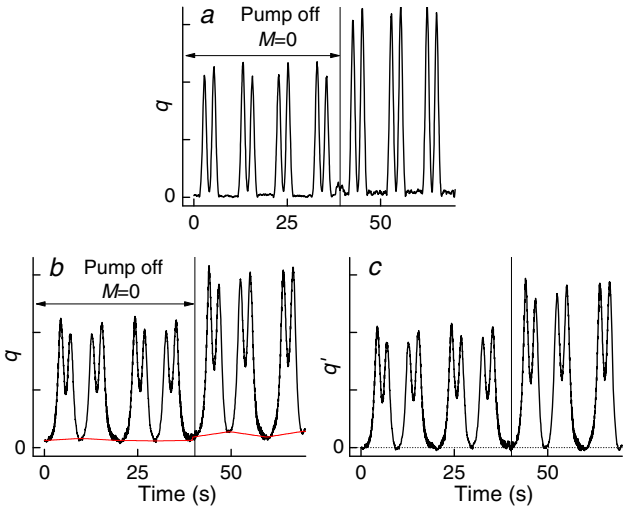

Fig. 4. Examples of low and high pressure probe spectra (1.33 mbar (a); 128 mbar (b, c)). (a, b) Time evolution of the modulation depth (q) for the first up and down frequency sweeps. Collisional broadening leads to line overlap and asymmetrical baselines (thin red lines in (b)). (c) Same data as in (b), after baseline correction (q'); dotted line: zero level.

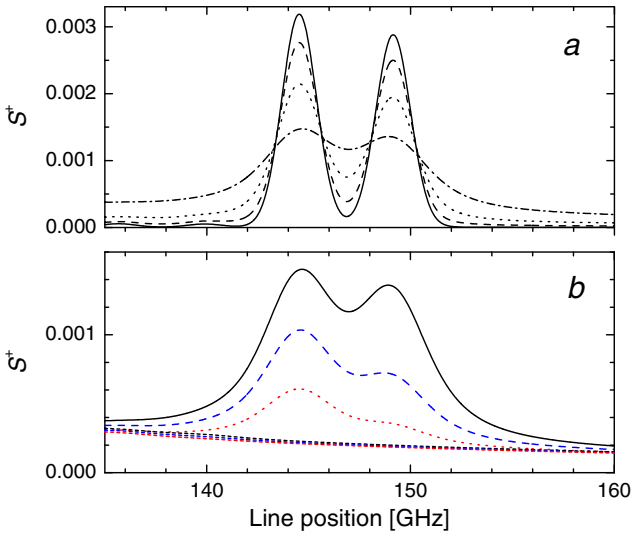

Fig. 5. Probe absorption spectra computed at 4.7 T and 300 K, for spin-temperature equilibrium (Eq. (8); fixed Gaussian FWHM $\overline{\omega}_{\rm G} = 1.978$ GHz). (a) $M = 0$, various Lorentzian FWHM values $\overline{\omega}_{\rm L}$: 0.0027 (solid), 0.038 (dash), 1.16 (dot), and 3.31 GHz (dash-dot). (b) Fixed $\overline{\omega}_{\rm L} = 3.31$ GHz, various M values: $M = 0$ (black solid), -0.25 (blue dash), and -0.5 (red dot). Short-dashed baselines: contributions of other σ^+ lines; from top to bottom: $M = 0$, -0.25, -0.5 (same line styles and colors).

The evolution of the spectrum with the Lorentzian FWHM $\overline{\omega}_{\rm L}$ can be observed in Figure 5a where spectral amplitudes S^+ computed for equally populated 2^3S sublevels are displayed. For $\overline{\omega}_{\rm L}/\overline{\omega}_{\rm G} \leq 0.5$ only a small fraction (in the percent range) of each peak height arises from other resonance lines. For larger FWHM ratio the contribution of the slanted baseline (9 and 23% for $\overline{\omega}_{\rm L}/\overline{\omega}_{\rm G} = 0.6$ and 1.7, respectively) is of the same order as that of the other probe line. The importance of the baseline contribution at large $\overline{\omega}_{\rm L}$ is more quantitatively illustrated in Figure 5b, where the computed doublet spectra and their (true) baselines are both displayed for various polarization values. The baselines are mildly affected by M but their relative contributions increase at high M since both peak amplitudes strongly decrease. It can be noticed on the graphs that the Lorentzian wings of the remote lines do not actually provide a linear baseline. It is also clear that the difference between the true baseline and a linear fit adjusted to the two end parts of the spectrum changes when M varies. As a result, a measurement of the frequency scan boundaries and detailed knowledge about the line shape and about the non trivial polarization-dependence of S^+ is needed to infer M and $n_{\rm m}^{\rm s}$ from the baseline-corrected peak amplitudes in a reliable way.

Finally, the experimental frequency scans are performed during build-up or decay. Therefore, polarization evolves in time and the recorded data cannot be directly compared to the spectra computed for fixed M. The method developed for data reduction involves numerical computations of S^+ at arbitrary M which are performed with experimental FWHM input values, obtained from Voigt line shape adjustments (Sect. 2.4.2). It provides tools for accurate measurements of the ^{3}He polarization with or without OP (Sect. 2.4.3) and of the 2^3S atom density in the polarized and unpolarized gas (Sect. 2.4.4) at all gas pressures. Technical details and underlying computations can be found in Appendix D.

2.4.2 2^3S-2^3P collisional broadening rate

The gas temperature (hence the Gaussian FWHM $\overline{\omega}_{\rm G}$) is a priori not accurately known in a MEOP experiment, where $T_{\rm gas}$ may exceed the room temperature because of the dissipated rf power. The ^{3}He number density N_0 is fixed for each OP cell and inside the closed volume the gas pressure p, proportional to $T_{\rm gas}$, may therefore exceed the cell filling pressure p_0. The Lorentzian FWHM $\overline{\omega}_{\rm L}$ depends on the collisional broadening rate of the 2^3S-2^3P transition for ^{3}He gas, for which presently no accurate value is available, and it varies both with gas density and temperature. The atomic linewidths are thus experimentally inferred from a quantitative analysis of the Voigt profile for the two probe lines. This provides the information needed for data reduction but also yields a body of experimental FWHM values for global assessment of the 2^3S-2^3P collisional broadening rate in ^{3}He.

The line shape measurements are performed using the data recorded at $M = 0$ before OP (e.g., the first four scans in Figs. 4a and 4b). Comparison is made with full absorption spectra computed for unpolarized pure ^{3}He gas[6],

[6] The cell cleaning and filling procedure is designed to yield a ^{4}He impurity level much smaller than the usual per mil value [15]. Moreover isotopic lines do not coincide at 4.7 T. The strongest ^{4}He lines would contribute to the σ^+ doublet baseline only for the 267 mbar cell where, anyhow, SNR is too low for detection or measurement of ^{4}He atom density by absorption.

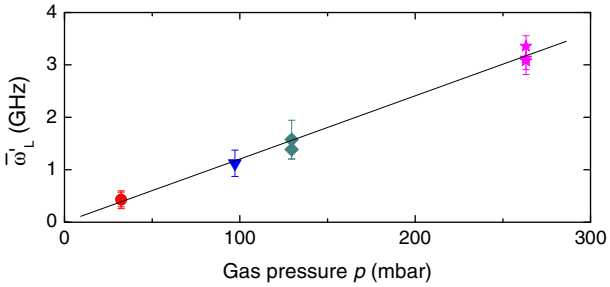

Fig. 6. Compilation of Lorentzian FWHM at $T = 300$ K. Symbols: T-scaled data obtained from the 4.7 T line shape measurements, using $\overline{\omega}'_{\rm L} = \overline{\omega}_{\rm L}(300/T^K_{\rm gas})^{0.353}$ and $p = p_0(300/T^{\rm K}_0)$ (Appendix B.3). Solid line: linear fit yielding the collisional broadening rate (slope) and base linewidth (intercept) of the 2^3S-2^3P transition.

over the probed frequency ranges (e.g., the part shown in Fig. 5a), to find the Voigt profiles that best fit the data. The adjustment procedure is described in the Appendix B.1. The doublet line splitting ($\nu_{1,10} - \nu_{2,9}$) provides a convenient absolute calibration of the frequency scale. The experimental scans typically span over 18 GHz. A pair of fit parameters ($T_{\rm gas}$, $\overline{\omega}_{\rm L}$) is obtained for each of the recordings performed in a given OP cell. At high pressure the sustainment of stable discharges requires more rf power and the inferred gas temperatures range up to $T_{\rm gas} = 350$ K. At intermediate pressure $\overline{\omega}_{\rm G}$ and $\overline{\omega}_{\rm L}$ have comparable values and $T_{\rm gas}$ is more difficult to determine accurately (uncertainty is $\delta T_{\rm gas} = \pm 10$ K despite the good signal-to-noise ratio, SNR). The quality of the Voigt adjustments is discussed in Appendix B.1.

The Lorentzian contribution to the Voigt line shape is significant and dominated by collisional broadening for the cells with $p_0 \geq 32$ mbar. Taking into account the dependence of the collisional width on $T_{\rm gas}$ (see Appendix B.3) the individual fit parameters $\overline{\omega}_{\rm L}$ are scaled in temperature for FWHM comparison at 300 K (Fig. 6). The compiled results are globally consistent. A linear fit to the scaled FWHM data yields a collisional broadening rate for pure ^{3}He gas at 300 K equal to:

$$\overline{\omega}'_{\rm L}/p = 12.0 \pm 0.4 \text{ MHz mbar}^{-1} \text{ FHWM}$$

and a residual FWHM at null gas pressure equal to $\overline{\omega}'_{\rm L}(0) = 10 \pm 1$ MHz. The latter reasonably matches the combined natural width of the atomic transition and emission bandwidth of the probe laser (the radiative lifetime of the 2^3P level yields $(1.021 \times 10^7 \text{ s}^{-1})/\pi = 3.25$ MHz FWHM [15]; the laser diode has a 3 MHz nominal bandwidth and a small frequency jitter).

The 2^3S-2^3P collisional broadening rates available in the literature are reported for the ^{4}He isotope only: 14−19 MHz mbar^{-1} FHWM for experimental work[7] [26–28] and 18.1 MHz mbar^{-1} FHWM at $T = 300$ K for theoretical work [29]. From mass-scaling arguments the broadening rate is expected to be 1.152 times larger for the ^{3}He atom, due to its higher thermal velocity at fixed temperature[8]. Hence, based on reference [29], it would be on the order of 21−22 MHz mbar^{-1} in pure ^{3}He for $T_{\rm gas}$ in the 300−350 K range. The ^{3}He line shapes measured in the present work thus lead to a consistently lower collisional broadening rate. Dedicated experiments at various controlled temperatures and other field strengths should be performed to address this quantitative discrepancy. A series of test measurements has been undertaken by two of the authors (G.T. and P.-J.N.) in the Earth field, for $p_0 = 8$–535 mbar over an extended range of temperature: 220−375 K. The line shape adjustments are performed over the whole 2^3S-2^3P absorption spectrum (C_1 to C_9 lines) and the preliminary result (12.5 ± 0.3 MHz mbar^{-1} FWHM at 300 K) is in agreement with the value obtained at 4.7 T with the σ^+ probe doublet scans.

The global linear fit displayed in Figure 6 is used to obtain the sets of best-fit parameters $T_{\rm gas}$ and $\overline{\omega}_{\rm L}$ listed in Table B.1 (Appendix B.2), where a single (most plausible) average value of $T_{\rm gas}$ is picked for each gas cell. The Voigt spectra computed with Table B.1 values actually provide excellent adjustments to all series of σ^+ doublet scans recorded at $M = 0$ in the 4.7 T experiments. These best-fit values are systematically used as input parameters for numerical computations and data reduction.

2.4.3 Nuclear polarization measurements

At spin-temperature equilibrium, the populations a_1 and a_2 of the probed Zeeman sublevels satisfy: $a_2/a_1 = e^\beta = (1+M)/(1-M)$. As long as this equilibrium prevails, the nuclear polarization is given by:

$$M = \frac{(a_2/a_1 - 1)}{(a_2/a_1 + 1)}. \tag{10}$$

Equation (10) holds both before OP (unpolarized gas, uniform a_i distribution: $a_1 = a_2 = 1/6$) and during polarization decay (pump beam blocked).

During OP, the pump light drives fast absorption − emission cycles and efficiently transfers atoms out of the pumped sublevels. The imbalanced distribution of populations enforced in the 2^3S state provides the driving term for the build-up of the nuclear polarization in the ground state [24]. M becomes negative for f_2^- pumping since the OP-induced skew is characterized by a strong depletion in A_5 and A_6 levels and excess populations in A_1 and A_2, with $a_1 \geq a_2$. As a result, the measured absorbances significantly increase for both probe lines when the OP beam is unblocked (Fig. 7a). However, numerical

[7] Accuracy is limited by the quality of the measurements in reference [26] (20 ± 5 MHz Torr^{-1}) and not specified in reference [27] (18.5 MHz Torr^{-1}, no T control). Reference [28] gives a more precise but unpublished value: 25.0 ± 0.2 MHz Torr^{-1}. (Original units.)

[8] Collision cross sections depend only on energy, hence on T, and are identical for both isotopes (except for quantum statistics effects, negligible at 300 K). Collision rates thus scale like velocities at fixed p and T, yielding $\overline{\omega}_{\rm L}(^3\text{He})/\overline{\omega}_{\rm L}(^4\text{He}) = \sqrt{M_4/M_3}$.

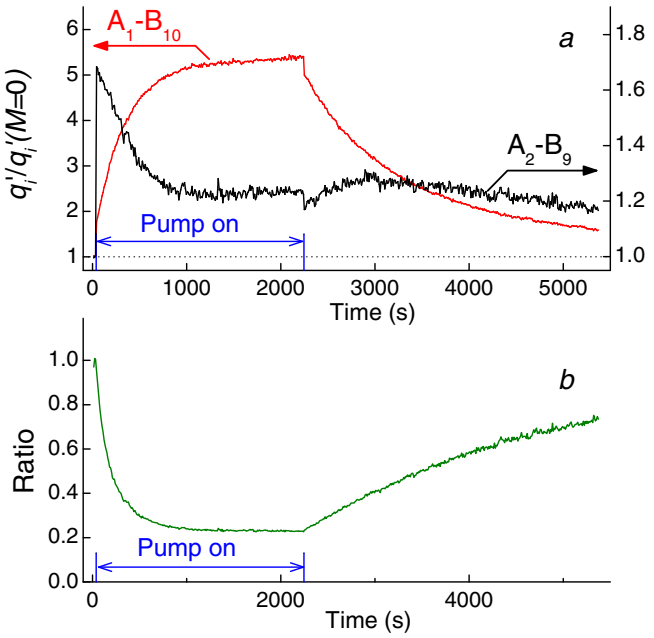

Fig. 7. (a) Time evolution of the baseline-corrected peak height q'_i, scaled to $M = 0$ value, for $i = 1$ (A_1-B_{10} line, red curve, left scale) and 2 (A_2-B_9 line, black curve, right scale). The M-dependent jumps observed at $t_{on} = 37$ s and $t_{off} = 2244$ s for both probe lines highlight the OP-induced changes of 2^3S sublevel populations. (b) The data set ratio $[q'_2/q'_2(0)]\times[q'_1/q'_1(0)]^{-1}$ (hence, a_2/a_1) exhibits no such discontinuity. Cancellation of fluctuations due to pump power noise provides good SNR. (Exp. conditions: 4.7 T, f_2^- OP, 0.5 W, $p_0 = 32$ mbar; $n^s_m = 3.5 \times 10^{16}$ m^{-3}.)

computations[9] performed at 4.7 T show that, as previously observed at 1.5 and 2 T [18,23], the ratio of populations is weakly affected by OP when the two sublevels belong to a pair of quasi-degenerate states (i.e., with $A_i(\infty) = |m_J, m_I = \pm 1/2\rangle$) that are not addressed by the pump laser. Hence, for f_2^- pumping the population ratio a_2/a_1 (for the probed $m_J = -1$ pair, see Tab. 1) or a_3/a_4 (for $m_J = 0$) remains nearly equal to its spin-temperature value and equation (10) can still be used for accurate measurements of M. For instance, at 267 mbar, the computed difference between a_2/a_1 (resp. a_3/a_4) and e^β does not exceed 1.9×10^{-4} (resp. 8.3×10^{-4}) for $-0.8 \leq M \leq 0$ for 2 W of OP light, whereas it rises up to 0.15 for a_5/a_6. This is confirmed experimentally by the absence of measurable differences in population ratio (Fig. 5b) or in M value when OP starts or stops (see Fig. 8, Sect. 2.5.1). From this point of view, the polarization measurements are easier to perform at high field than at low field where dedicated experiments must be carried out to measure, at fixed operating conditions, the OP-induced change in probe light absorbance for many values of M [19].

In order to use equation (10), with or without OP, a measurement of a_2/a_1 is needed. The probe laser frequency is alternatively tuned to the A_2-B_9 and A_1-B_{10} lines. Comparison of peak absorbances is straightforward at steady state, namely when $M = 0$ (before OP or after full decay of M) or when M is close to the stationary value that is asymptotically reached with OP. During build-up or decay, an interpolation is required to evaluate both absorbances at the same time point in the evolution of M [16,18]. This is performed off-line by an in-house compiled program that analyses the successive baseline-corrected spectra, extracts a discrete series of time and amplitude values for the two resonance lines, and provides for each scan an average time abscissa, t, and interpolated peak heights, q'_2 and q'_1, for A_2-B_9 and A_1-B_{10} (respectively), as well as two dimensionless quantities:

$$r_{21} = \frac{q'_2}{q'_1}\frac{T_{1,10}(\sigma^+)}{T_{2,9}(\sigma^+)} \tag{11}$$

and

$$M^{\rm raw} = \frac{(r_{21}-1)}{(r_{21}+1)}. \tag{12}$$

At low pressure (up to a few millibars) no baseline correction is needed: $q'_i = q_i \propto L_{\rm path} n^s_m \tilde{\sigma} a_i T_{ij} I_{\rm Voigt}(0)$. The quantity r_{21} reduces to the ratio of populations ($r_{21} = a_2/a_1$) and the nuclear polarization is simply inferred as:

$$M = M^{\rm raw}. \tag{13}$$

At high pressure, because of the line overlap, the output value $M^{\rm raw}$ significant differs from the (true) polarization M. The quantitative link between $M^{\rm raw}$ and M is pragmatically established numerically at fixed atomic linewidths (i.e., for each cell) and the nuclear polarization is obtained as:

$$M = M^{\rm raw} + \delta M^{\rm corr}(M^{\rm raw}). \tag{14}$$

The method used to compute the difference $\delta M^{\rm corr} = M - M^{\rm raw}$ as a function of $M^{\rm raw}$ is described in Appendix D.1, and the results obtained at 4.7 T are shown in Figure D.2 (see Fig. D.4 in Appendix D.3 for other B values). As expected, $\delta M^{\rm corr}$ increases monotonically with M. It rises with the gas pressure and becomes large for the highest p_0 values. In the conditions of the experiment $|M^{\rm raw}|$ systematically underestimates the ^{3}He polarization ($M < M^{\rm raw} < 0$, see Fig. 8 in Sect. 2.5.1). The relative magnitude of the correction, $\delta M^{\rm corr}/M^{\rm raw}$, typically ranges from less than 2.7% at 32 mbar to 26% at 267 mbar for $M^{\rm raw} = -0.30$, for instance. Hence, in practice, $M^{\rm raw}$ provides a fairly good approximation of M at moderate pressure but $|M^{\rm raw}|$ only yields a lower bound for $|M|$ at high pressure. Equation (14) and an analytical expression of $\delta M^{\rm corr}$ are needed for accurate polarization measurements in both cases.

[9] An improved MEOP model is used [14,24], based on the 2^3S and 2^3P level structure and on the OP and ME description given in reference [15]. Full collisional mixing is assumed in the 2^3P state (Dehmelt regime) and, as in reference [2], relaxation in the 2^3S and 1^1S states is phenomenologically taken into account.

2.4.4 Metastable density measurements

The 2^3S atom density is inhomogeneous inside the MEOP cells. It necessarily vanishes at the walls, where all metastable atoms de-excite. In the bulk, the competition between the pressure dependent formation and quenching processes leads to a spatial distribution that depends on the rf excitation pattern, varies with the experimental conditions, and cannot be reliably inferred from the emission of visible fluorescence light by the plasma. The bone-shaped cells have a large aspect ratio and extended electrode wirings. One may reasonably consider $n_{\rm m}$ to be uniform along the tube axis and neglect the local effect of its decrease near the end windows. But this is not legitimate in the transverse plane. Absorption measurements at low magnetic field show an evolution from a bell-shaped radial profile at low p_0 (with a broad maximum on the axis) to annular ones at high p_0 (with a strongly depleted central area). Quantitative 2D mappings have been performed at 2 T for moderate and high p_0 [17]. The radial profiles are fairly flat at 32 mbar and exhibit gradually sharper maxima near the tube wall, with $n_{\rm m}$ values typically 3 (resp. 5 and 23) times larger than those measured on the axis at 67 (resp. 96 and 128) mbar. For MEOP, the inhomogeneous distribution of 2^3S atoms leads to a strong variation of the local pump absorption rates[10] but atomic diffusion ensures uniform gas polarization (diffusion times for ground state atoms [30] are short compared to M build-up and decay times) [2,15,24].

Static measurements

The probe absorbance provides an average value of the number density of 2^3S atoms equal to:

$$n_{\rm m}^{\rm s} = \frac{1}{L_{\rm path}} \int_{\rm path} n_{\rm m}(l) dl, \tag{15}$$

where l is the linear abscissa along the probe path and $n_{\rm m}(l)$ the local number density. This actually corresponds to the average of the transverse distribution over the sampled fraction of the cell radius (Appendix C, Eq. (C.3)) which, by design, is quite large (typically 70%) and excludes only a 0.6 mm-wide part at the center. Therefore, $n_{\rm m}^{\rm s}$ provides a useful estimate of the fraction of ^{3}He atoms promoted to the 2^3S state by the rf excitation and illuminated by the pump beam during OP. The $n_{\rm m}^{\rm s}$ values reported in Section 3.1 are obtained in the unpolarized gas by static, absolute absorbance measurements (at fixed laser diode frequency, steady-state plasma conditions, and constant $M = 0$ value), using the time-integrated probe signal for comparison of $\mathcal{P}_{\rm on}$ and $\mathcal{P}_{\rm off}$ for one atomic line. Equation (9) is used for data reduction, together with the computed peak values of S^+ listed in Table B.2 (Appendix B). The explicit dependence of the cross-section prefactor $\tilde{\sigma}$ on $T_{\rm gas}$ is duly taken into account (Eq. (6)).

Unfortunately, no such direct information on the 2^3S atom density can be obtained from OP light absorption, due to the transverse extension of the pump beam and its broad spectral width (see Appendices C.2 and C.3). However, the additional static measurements that are performed before OP, with the fiber laser at very low power, yield light transmittance values $\mathcal{T}_{\rm pump}^{\rm att.}$ that further characterize (globally) the plasma conditions and indirectly probe the overlap between the radial profiles of the 2^3S atom distribution and of the OP light intensity (Appendix C, Eqs. (C.14) and (C.17)). This quantitative element of information is relevant for the MEOP dynamics, hence for interpretation of the experimental results.

The probe beam is weakly absorbed by the plasma ($1 - \mathcal{T}$ typically ranges from 6% at 1.33 mbar to 0.4% at 267 mbar) since the T_{ij} matrix elements are about ten times smaller for the A_2-B_9 probe line used at 4.7 T than for the C_8 or C_9 line used at low field (2^3S-2^3P$_0$ transition). Spectral amplitudes are 100 times larger when the laser diode is tuned to the f_2^+ line, for instance, which substantially increases the accuracy of the static $n_{\rm m}^{\rm s}$ measurements. The relative errors on $n_{\rm m}^{\rm s}$ vary from 5 to 15% (depending on cell content) for the A_2-B_9 line and from 0.2 to 1% for the f_2^+ line. The measurements performed with the OP beam yield reasonably high $\mathcal{T}_{\rm pump}^{\rm att.}$ values. However, they are much less accurate because of the large output power noise of the fiber laser.

Finally, the static light absorption measurements are performed prior to the recording of OP dynamics. Tests show that identical rf levels sometimes fail to yield the same results if the discharge is switched off between measurements. This has been observed at various field strengths above 0.1 T (and by several groups) and may also contribute to the scatter of the experimental data. The demodulated signal amplitudes at $M = 0$ should allow direct comparison of the plasma conditions within each experimental run. They do not provide reliable checks in the present work because the modulation depth of the rf driving voltage has not been systematically assessed, which potentially limits the quality of a few individual results. Nevertheless, the collected data are globally consistent and the plasma characteristics measured at 4.7 T are satisfactorily in line with previous findings.

Dynamic measurements

The demodulated component of the probe signal is used to quantitatively monitor the relative changes in $n_{\rm m}$ during polarization decay, assuming that the modulation depth of the discharge intensity does not vary much with M. Such changes, mainly due to a modification of the 2^3S atom de-excitation rate by Penning auto-ionization (sensitive to the electronic orientation), are consistently observed in MEOP experiments [13,15,24,31]. Since spin-temperature equilibrium is established in the absence of OP, the relative change in average 2^3S atom density $v_{\rm m}$ can be inferred from the ratio of one peak absorbance (q_i with $i = 1$ or 2) measured at polarization M to the value obtained at $M = 0$, using equation (9):

$$v_{\rm m} = \frac{n_{\rm m}^{\rm s}(M)}{n_{\rm m}^{\rm s}(0)} = \frac{q_i(M)}{q_i(0)} \frac{S_i^+(0)}{S_i^+(M)}, \tag{16}$$

[10] A detailed mapping of $n_{\rm m}$ would thus be required, e.g., for accurate modeling of the MEOP dynamics.

where $S_i^+(M)$ stands for the value of $S^+(\nu_{ij})$ for ^{3}He gas with polarization M. This requires the knowledge of M at the time at which the peak value is reached, as well as an accurate analytical expression of $S_i^+(M)$.

Alternatively, one can use the output quantities of the data processing program (interpolated time abscissa t, baseline-corrected peak height q_i', apparent polarization $M^{\rm raw}$), which are used for the gas polarization measurements and similarly proceed in two steps: (i) an approximate value, $v_{\rm m}^{\rm raw}$, is obtained using the low pressure limit (for which $S_i^+(0)/S_i^+(M) = a_i(0)/a_i(M)$):

$$v_{\rm m}^{\rm raw} = \frac{q_i'(M)}{q_i'(0)} \frac{a_i(M_0^{\rm raw})}{a_i(M^{\rm raw})}, \tag{17}$$

where $a_i(M^{\rm raw})$ is the population that would be established at spin-temperature equilibrium in a gas with polarization $M^{\rm raw}$ and $M_0^{\rm raw}$ denotes the value of $M^{\rm raw}$ for $M = 0$; (ii) the correction function $v_{\rm m}^{\rm corr}$, defined as:

$$v_{\rm m}^{\rm corr} = v_{\rm m}/v_{\rm m}^{\rm raw} \tag{18}$$

is computed, once, for each cell and used to obtain a more accurate value of $v_{\rm m}$ at high gas density. The magnitude and M dependence of $v_{\rm m}^{\rm corr}$ at 4.7 T is described in Appendix D.2 (Fig. D.3; see Fig. D.5 in Appendix D.3 for other B values). Thanks to the modulation technique, the SNR is good enough for reliable measurements of the relative changes of $n_{\rm m}^{\rm s}$ in spite of the low probe light absorbances obtained at 4.7 T with the σ^+ line doublet.

2.5 Characterization of MEOP dynamics and efficiency

2.5.1 Analysis of MEOP dynamics at 4.7 T

Figure 8 displays an example of reduced data obtained from a recording of the absorption signals during polarization build-up and decay. The difference between $M^{\rm raw}$ and M (Fig. 8a) is indicative of the effect of the pressure dependent overlap of the resonance lines. The absence of discontinuity in the time evolution of M when OP starts and stops confirms the expected robustness of the population ratio a_2/a_1 against the perturbation introduced in the 2^3S state by the OP light.

The build-up plot (Fig. 8b) shows that M approaches its steady-state value $M_{\rm SS}$ in a truly exponential way. This is observed in all gas cells and plasma conditions. It is a striking feature of MEOP experiments performed at 4.7 T. It allows a full description of the polarization build-up dynamics by only two parameters, the steady-state polarization $M_{\rm SS}$ and the constant build-up rate $\Gamma_{\rm OP}$:

$$M(t) = M_{\rm SS}(1 - \exp\{-\Gamma_{\rm OP}\,(t - t_{\rm on})\}) \tag{19}$$

if OP starts from $M = 0$ at time $t = t_{\rm on}$ for instance. When MEOP is performed at lower field, the build-up rates are observed to vary in time (Eq. (28), Sect. 3.4.2) and to decrease when M approaches $M_{\rm SS}$ [3,16,18,24,32].

The decay plot (Fig. 8c) shows that M decreases exponentially towards zero as soon as the OP beam is blocked.

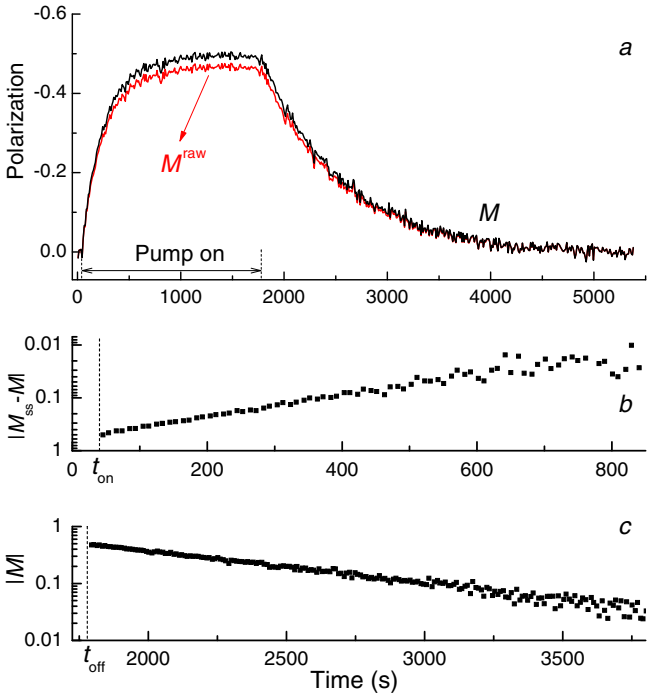

Fig. 8. Example of experimental data showing MEOP dynamics at 4.7 T. OP starts from $M = 0$ at $t_{\rm on} = 40.3$ s and stops at $t_{\rm off} = 1779$ s. (a) Difference between $M^{\rm raw}$ (red bottom line, see text) and M (black top line) increases with $|M|$. No discontinuity is observed at $t_{\rm on}$ or $t_{\rm off}$. (b) Semi-log plot of M build-up. Approach to steady-state value is exponential (Eq. (19)): $M_{\rm SS} = -0.491 \pm 0.001$, $\Gamma_{\rm OP} = (4.76 \pm 0.04) \times 10^{-3}$ s^{-1}. (c) Semi-log plot of M decay. Decrease towards $M = 0$ is exponential (Eq. (20)): $\Gamma_{\rm D} = (1.310 \pm 0.009) \times 10^{-3}$ s^{-1} (Exp. conditions: f_2^- OP line, 0.5 W laser power; 128 mbar cell, $n_{\rm m}^{\rm s} = 1.9 \times 10^{16}$ m^{-3}).

If, as here, polarization decay starts from steady-state value at time $t = t_{\rm off}$ the time evolution reads:

$$M(t) = M_{\rm SS} \exp\{-\Gamma_{\rm D}\,(t - t_{\rm off})\} \tag{20}$$

where $\Gamma_{\rm D}$ is the decay rate measured in the plasma in the absence of OP light. Polarization decays are exponential in all experiments performed at 4.7 T. This has been systematically observed, so far, at any other field strength as well. The decay rate $\Gamma_{\rm D}$ is a parameter that further characterizes, indirectly, the plasma conditions established for MEOP by the rf excitation. It always exceeds the relaxation rate that would be measured in the gas without rf discharge. $\Gamma_{\rm D}$ generally increases with the applied rf power in a way that strongly depends on the experimental conditions (cell geometry, electrodes configuration, gas pressure, field strength, etc.). It is usually correlated to the average 2^3S atom density at fixed gas pressure. However, there is, to date, little information about this apparent link and no indication of its physical origin. The plasma conditions are always pragmatically optimized to obtain the best efficiency.

The global parameters $n_{\rm m}^{\rm s}$ and $\Gamma_{\rm D}$ are related to plasma-induced quantities that play distinct roles in

MEOP. The 2^3S atom density determines both the amount of OP light that is locally absorbed by the plasma (hence the 2^3S-2^3P OP rate and, consequently, the nuclear polarization of the 2^3S atoms) and the local ME rate. It thus strongly impacts two factors jointly involved in the average flow rate of angular momentum into the ground state [24], i.e., the ME-driven source term for the time evolution of M (Eq. (25), Sect. 3.2). The decay rate Γ_D measures an overall loss rate of nuclear polarization in the plasma that accounts for all processes irreversibly driving M towards zero in the absence of OP (which includes the relaxation processes directly acting on the 1^1S atoms and the average ME-driven contribution of 2^3S relaxation). It essentially limits M_{SS} for MEOP at low pump power [2,24].

2.5.2 Parameters used to characterize MEOP efficiency

The two basic experimental results for polarization build-up (steady-state value M_{SS}, constant rate Γ_{OP}) can be analyzed in various ways, depending on the targeted application of the MEOP technique (use of polarized ^{3}He gas for nuclear physics, neutron physics, magnetometry, or NMR; development of polarizers for massive production of high grade polarized ^{3}He gas; optimization of MEOP cells as sources of polarized electrons). They can be advantageously combined to infer quantities that are more relevant for this targeted application and, hence, better suited to assess the "efficiency" of MEOP. For instance, when ^{3}He is used as a polarizing or analyzing neutron spin filter, the filter transmittance T_f and the outgoing neutron polarization P_n are key parameters. The optimization of the figure of merit $T_f P_n^2$ requires large quantities of dense gas but also extremely high ^{3}He polarizations[11]. For NMR, the available signal is proportional to the magnetic moment of the ^{3}He sample, i.e., to the product of the nuclear polarization, the gas number density, and the volume of the sample. A high polarization is requested when the amount of ^{3}He used in the experiment is limited, e.g., by the cost or the availability of ^{3}He. More often, the sample size is fixed and the end-user needs gas with the largest possible magnetization. For a given design of the OP, gas handling, and storage systems, the producer's challenge then lies in the optimization of the operating conditions inside the OP cell(s) and in the choice of the best production scheme (batch mode or continuous flow)[12].

The evaluation of the efficiency of the MEOP process may then involve, with a rank that is assigned according to the final objective, the following combined quantities:

- *Nuclear magnetization,* MN_0. In the steady state the magnetization produced in the cell is equal to $M_{SS}N_0$ (N_0: ^{3}He density, constant in a sealed volume).
- *Pumping time,* $\tau_{OP} = 1/\Gamma_{OP}$. It provides a convenient characteristic time scale for MEOP. For instance, if OP starts at $t = 0$ from $M = 0$, M already reaches 86% of its steady-state value at $t = 2\tau_{OP}$.
- *Pumping speed,* $\dot{M}(t) = dM/dt$. The growth of M starts with an initial pumping speed:

$$\dot{M}(0) = \Gamma_{OP} M_{SS}. \tag{21}$$

Relaxation comes into play at finite M and competition between OP and depolarization during build-up leads to a pumping speed that varies as:

$$\dot{M} = \Gamma_{OP}(M_{SS} - M). \tag{22}$$

In a sealed cell $\dot{M}(0)$ is an intensive quantity that essentially depends on pressure and on plasma conditions through the 1^1S and 2^3S atom densities N and n_m, respectively ($n_m \ll N \simeq N_0$ in all MEOP experiments). The variation with the 2^3S atom density is mainly due to the fact that the angular momentum deposited by OP is transferred to the 1^1S atoms with a ME rate proportional to n_m. A small indirect contribution arises from the fact that the amount transferred per ME collision (the OP-induced excess nuclear polarization of the 2^3S atoms) depends on the local absorbed OP light power [5,24].

- *Magnetization build-up speed,* $R_{[M]} = |\dot{M}(t)|N_0$. This corresponds to the amount of magnetization produced per unit time, another intensive quantity which is relevant in massive production of hyperpolarized ^{3}He gas. $R_{[M]}$ steadily decreases during OP, starting from the initial magnetization build-up speed, $R_{[0]}$:

$$R_{[0]} = \Gamma_{OP} |M_{SS}| N_0, \tag{23}$$

and can be inferred at arbitrary M during build-up, using:

$$R_{[M]} = R_{[0]} - M\Gamma_{OP}N_0. \tag{24}$$

In Section 3 the experimental results are first reported in terms of M_{SS} and Γ_{OP}. The intensive quantities $|M_{SS}|N_0$, $\dot{M}(0)$, and $R_{[0]}$ are then used to discuss and compare MEOP efficiency in various operating conditions.

3 Results

In order to permit a reliable comparison of efficiency for different gas densities, the investigation carried out at 4.7 T involves measurements performed in discharge and pumping conditions that are currently typical of high-field MEOP operation. The effect of the rf excitation level is assessed through a quantitative analysis of the plasma characteristics in Section 3.1 and of the OP results obtained at fixed laser power (0.5 W) in Section 3.2. The results obtained at different laser powers (0.5, 1 and 2 W) are presented in Section 3.3. The efficiency of MEOP is then globally evaluated, at 4.7 T and other field strengths, in Section 3.4, where the discussion focuses on

[11] $T_f = \exp(-NL_f\Sigma_n)\cosh(MNL_f\Sigma_n)$, $P_n = \tanh(MNL_f\Sigma_n)$. N: ^{3}He density, L_f: length of the spin filter cell, Σ_n: cross section for unpolarized neutron capture [33].

[12] For the OP process, operation in batch mode or with sealed cells is equivalent. However, gas flow modifies the dynamics of M growth, as briefly outlined in Section 3.4.1.

the optimization of the operating conditions in view of applications.

It should be noted that the values of the laser power given in the text correspond to the OP light power incident on the cell. In the double-pass configuration the ^{3}He gas is submitted to an effective pump power which is higher (not exactly two times larger, because part of the pump light is absorbed by the plasma) and, as usual, difficult to compute accurately [2,15,24].

So far the OP cells have been designated by rounded values of their filling pressure, as usual. Since the operating pressure during MEOP differs from p_0 (by up to 16% in the 267 mbar cell), the fixed content is better characterized by the ^{3}He density. N_0 is also an intensive quantity that is mostly relevant for the OP dynamics and for comparison to n_m, as well as for various applications of hyperpolarized ^{3}He. Therefore, the results are systematically reported in terms of N_0 and the cell content is specified by a rounded N_0 value (which simply differs from p_0 value by a factor one thousand, roughly, with the choice of millibar and amagat units). The exact values of N_0 and p_0 are provided in Appendix B (Tab. B.1, Sect. B.2).

Finally, for clarity the same symbol shape (and color, for the electronic version) is assigned to each OP cell for all graphs in Section 3 and in Appendices B–D (0.001 amg: black squares; 0.03 amg: red dots; 0.06 amg: green up triangles; 0.09 amg: blue down triangles; 0.12 amg: dark cyan diamonds; 0.25 amg: magenta stars). This assignment is recalled in the figure caption when selected data are displayed and it appears in a graph legend with p_0 values when data are compiled with a density axis.

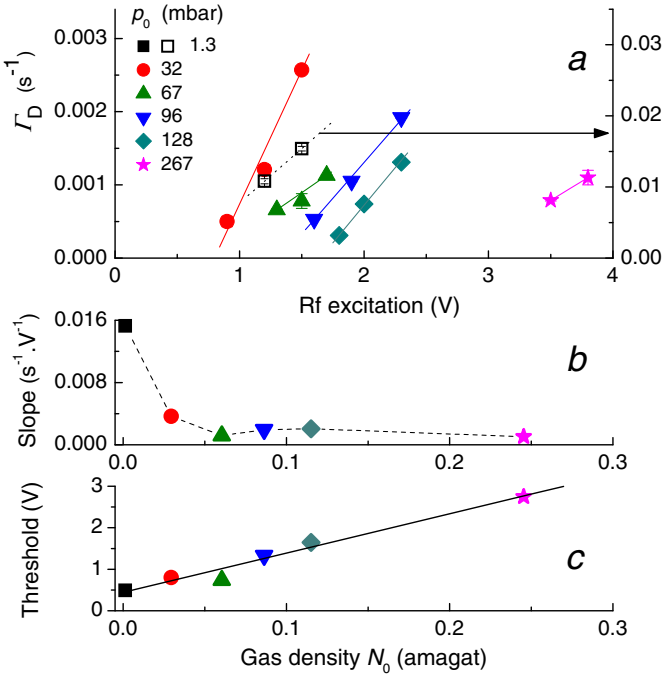

Fig. 9. Polarization decay rates Γ_D measured in the plasma (4.7 T, no OP). (a) Variation of Γ_D with the rf driving voltage (symbols; most error bars are smaller in size). A different scale (right axis) is used for 0.001 amg, as indicated by the pointing arrow and the use of open squares and dotted line. Straight lines: linear fits to the data obtained at fixed N_0. The fit slopes (b) (connecting dashed line: guide for the eye) and horizontal intercepts (c) (straight solid line: linear fit) are plotted in the lower panels.

3.1 Plasma conditions

At moderate or high gas density ($N_0 \geq 0.03$ amg) fairly long decay times are obtained at 4.7 T ($1/\Gamma_D$ = 500–2000 s, see Fig. 9) in comparison with standard low field values, in spite of the stronger rf excitation needed to sustain stable discharges and to reach suitable 2^3S atom densities ($0.5–8 \times 10^{16}$ m^{-3}, see Fig. 10). Much faster nuclear relaxation ($1/\Gamma_D$ = 80–150 s) occurs in the 0.001 amg cell for comparable rf levels. The high decay rates are presumably not caused by a contamination of the ^{3}He gas since fairly high n_m^s values are obtained: $8–14 \times 10^{16}$ m^{-3} (impurities would efficiently quench the 2^3S atoms). Strong depolarization may occur at the walls in this particular cell, which would need to be confirmed but can be expected to have a significant impact on global decay.

The decay rate Γ_D is observed to increase linearly with the driving rf voltage applied to the linear power amplifier (Fig. 9a; note the change in vertical scale for 0.001 amg). Slope (Fig. 9b) and intercept (Fig. 9c, indicative of discharge threshold) vary in opposite ways when density increases. They jointly describe the increasingly difficult spontaneous ignition of rf discharges at high N_0. There is a striking difference between the behaviors exhibited by the Γ_D increase rate for $N_0 \geq 0.06$ amg (fit slopes, roughly independent of density, are equal to 1.6×10^{-3} s^{-1} V^{-1} on average) and below 0.06 amg (fit slope is 2.6 and 10 times larger for N_0 = 0.03 and 0.001 amg, respectively). This may indicate that, in spite of the identical cell shape and electrode configuration, a different plasma regime is achieved at 0.001 amg. Altogether the efficiency of 4.7 T MEOP can be investigated at moderate and high density with fairly comparable decay rates Γ_D, in the $0.5–1.5 \times 10^{-3}$ s^{-1} range.

Metastable atom densities exhibit a monotonic but limited increase with the rf excitation level at fixed gas density. The graph in Figure 10a shows the correlation between the average 2^3S atom density n_m^s and the decay rate Γ_D for all investigated rf plasmas. The plotted data sets exhibit consistent behaviors, typical for MEOP experiments carried out with fixed cell size and electrode configuration: a stronger rf excitation progressively leads to a smaller increase in n_m^s, ultimately yielding a strongly enhanced Γ_D with no further increase of n_m^s (an unfavorable plasma regime usually reached only for strong discharge intensities in standard MEOP conditions). In Figure 10a the probed range of 2^3S atom density can be observed to decrease when N_0 increases. The relative span is about the same, but the various n_m^s ranges hardly overlap for low (0.001 amg), moderate (0.03−0.09 amg), and high (0.12−0.25 amg) density. As a result, the proportion of ^{3}He atoms in the 2^3S state drops dramatically by three orders of magnitude (n_m^s/N_0 ratio, Fig. 10b), from a few

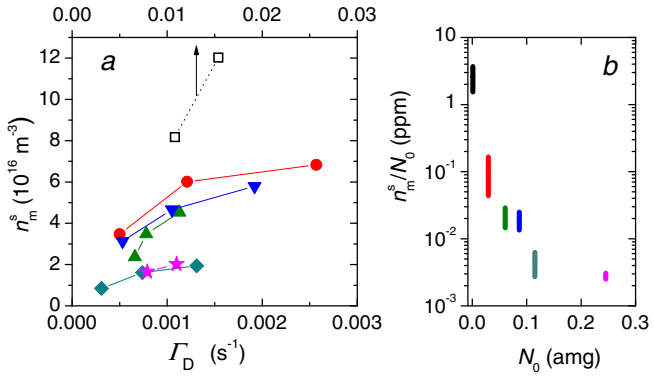

Fig. 10. 2^3S atom densities measured at 4.7 T for $M = 0$. (a) Correlation between average density n_m^s and decay rate Γ_D for various rf excitation levels (legend: see Fig. 9a; error bars are not shown for clarity). (b) Fraction of atoms promoted to the 2^3S state versus gas density (same data sets; the bar symbols extend from min. to max. values).

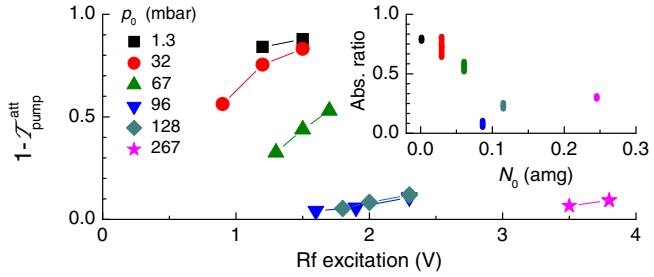

Fig. 11. Fraction of light power absorbed from a low-power pump beam at $M = 0$ with the f_2^- line at 4.7 T. Main plot: variation with rf excitation and cell content (legend: see Fig. 9a). Inset: Same data sets, scaled to the values computed for a narrow beam (from the data in Fig. 10, see text); the bar symbols extend from min. to max. values.

parts per million at 0.001 amg (as usually obtained in low-field MEOP) to parts per billion at 0.25 amg.

Figure 11 shows the fraction of light power absorbed by the same plasmas, at very low laser power, when the measurements are performed with the wide OP beam. As expected, the results are in qualitative agreement with those obtained with the probe beam: light absorption is systematically enhanced when the rf excitation level increases and it is much stronger for low than for high gas density (Fig. 11, main plot). However, the variation of $1 - \mathcal{T}_{pump}^{att.}$ with N_0 apparently depends on the density range: up to 0.06 amg the measured values are fairly high and gradually decrease when N_0 rises; between 0.09 and 0.25 amg they are low (4–12%) and do not vary much with N_0. The interpretation of this behavior is not straightforward, due to the joint contributions of the global change in n_m values and of the mismatch in radial profile between the 2^3S atom density and the light intensity (see Appendix C.3). A way to estimate the relative impact of each contribution is to compare $1 - \mathcal{T}_{pump}^{att.}$ to the value expected for a strongly diaphragmed beam with identical spectral width, propagating along the cell axis in a gas with a 2^3S atom density

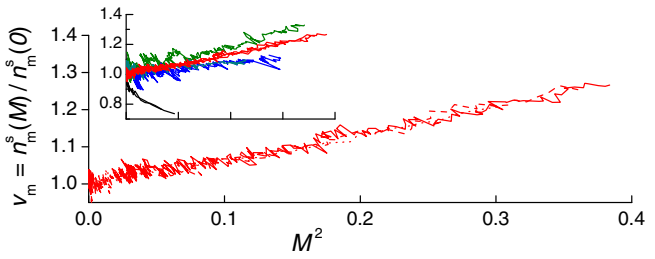

Fig. 12. Changes in 2^3S atom density during polarization decay (4.7 T, no OP). Main plot: $N_0 = 0.03$ amg. Plotted against M^2, the relative density change v_m exhibits an identical linear increase for 3 rf levels (solid, dash, and dot lines, overlapped). Inset: data compilation (v_m vs. M^2, same horizontal axis). From top to bottom: 0.06 (green line), 0.03 (3 red lines), 0.09 and 0.12 (blue and dark cyan lines, overlapped), and 0.001 amg (2 black lines).

equal to n_m^s.[13] A compilation of the results (Fig. 11, inset) shows, first, that the correlation between $1 - \mathcal{T}_{pump}^{att.}$ and n_m^s is strong for fixed N_0: the computed ratio between $1 - \mathcal{T}_{pump}^{att.}$ and the value expected for the diaphragmed beam hardly depends on the applied rf voltage, while n_m^s typically varies by a factor 2.5 (see Fig. 10). The compilation also shows that this ratio is always smaller than one (a systematically lower fraction of light power is absorbed for the wide beam) and particularly low for $N_0 \geq 0.09$ amg. This suggests that the spatial inhomogeneity of the 2^3S atom distribution plays an increasing (and negative) role in the change of $1 - \mathcal{T}_{pump}^{att.}$ at high gas density, which presumably leads to reduced pump light absorption and MEOP efficiency.

Finally, a significant variation of the average 2^3S atom density with the ^{3}He nuclear polarization is systematically observed. The relative density change v_m is independent of the rf excitation level in a given cell (Fig. 12, main plot) but it varies noticeably with the gas density (Fig. 12, inset). These changes are comparable in magnitude with those observed at somewhat lower magnetic field [18,24] and do not exceed 30% for the highest polarization values. Auto-ionization is forbidden between 2^3S atoms with parallel spins (because of spin conservation) independently of the sign of their orientation. Density changes are thus expected to be even functions of the electronic polarization J_z and hence, approximately, of M, because $J_z = 4M/(3 + M^2)$ at spin-temperature equilibrium [24]. The experimental data roughly scale linearly with both J_z^2 and M^2 at all gas densities. If the main plot (0.03 amg) is used as reference, the slope of the v_m increase is larger at 0.06 amg and smaller at 0.09 and 0.12 amg. No significant change is observed at 0.25 amg (data not shown) but the quality of the results is limited by the poorer SNR and lower M values obtained in this cell. A surprisingly large variation (with opposite initial slope and small departure from linear behavior) is observed

[13] The probe absorbance values that yield the n_m^s data in Figure 10 are first scaled up to account for the difference in line spectral amplitudes (Appendix C.1), then corrected for the difference in laser bandwidth (Appendix C.2).

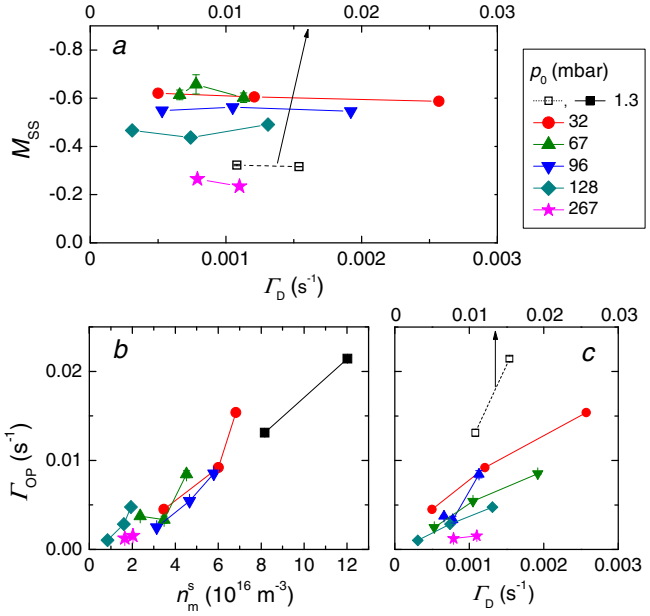

Fig. 13. Compilation of results obtained with 0.5 W laser power for various plasma conditions (4.7 T, f_2^- OP line). (a) Steady-state polarization vs. decay rate. (b, c) Build-up rate vs. 2^3S atom density and decay rate, respectively.

at 0.001 amg. This finding remains to be experimentally confirmed, at 4.7 T and other high field strengths. At low and moderate field, for a similar gas density, the sign and amplitude of v_m have already been observed to vary both with rf excitation level and operating conditions. The reported values range from −10% at $M = 0.8$ (decreasing at high rf levels) for $B = 0.5$–5 mT [31] to +2% at $M = 0.5$ for $B = 0.1$ T [15], for instance, in a 5 cm diameter ^{3}He cell with 1 mbar pressure and two ring electrodes.

3.2 Results obtained with 0.5 W of laser power

For each OP cell, a compilation of the results obtained at fixed pump power allows an evaluation of the impact of the plasma conditions. Figure 13 displays the values of the steady-state polarization M_{SS} and build-up-rate Γ_{OP} obtained at 4.7 T for f_2^- OP with 0.5 W of incident light power. At fixed gas density M_{SS} hardly depends on the decay rate measured in the plasma without OP (Fig. 13a). This means that M_{SS} is globally not influenced by the rf level and, hence, does not depend on n_m^s either. It also suggests that, during OP, nuclear relaxation may be dominated by a process yielding a loss rate much higher than Γ_D, as observed at lower field [16,24]. In contrast, the build-up rates strongly vary with the rf level (Fig. 13, lower panel). If the whole set of data is considered, irrespective of cell contents, the changes in Γ_{OP} seem to correlate better with those of the 2^3S atom density (Fig. 13b) than with those of the decay rate (Fig. 13c).

Recently a fairly simple approach of MEOP dynamics has been proposed, based on a global angular momentum budget for the atomic system [24]. In the rate equation describing the time evolution of M, the pumping speed is obtained as the net difference between a driving OP term (the rate at which nuclear orientation is transferred from the OP light to the 1^1S atoms, through ME collisions with the polarized 2^3S atoms) and of a loss term (the rate at which orientation is destroyed by relaxation processes). The input rate of angular momentum is determined by the global efficiency of the OP cycles and increasingly sophisticated models have been developed to quantitatively account for all relevant processes: laser-induced 2^3S-2^3P transitions, spontaneous emission, redistribution between Zeeman sublevels (by collisions or other interactions), ME exchange with the 1^1S atom reservoir. Even if a coarse phenomenological description of the redistribution of populations is used, solving the system of (coupled, local, and non linear) rate equations for ME, OP, and relaxation is a difficult task that involves several ill-known parameters. Very pragmatically and with no need for further model description, the rate equation for M can be written as:

$$\frac{dM}{dt} = 2\eta \frac{W_{abs}}{NV_{cell}\hbar\omega_{OP}} - \Gamma_R M. \quad (25)$$

In the right-hand side of equation (25) the first term is the OP contribution to M growth. It simply involves the product of the number of absorbed photons, $W_{abs}/\hbar\omega_{OP}$ (W_{abs}: absorbed pump power, a measurable quantity; $\hbar\omega_{OP}$: energy of the driven 2^3S-2^3P transition, a known quantity) and the so-called photon efficiency of the OP line η (the amount of angular momentum deposited in the gas by each absorbed photon; it only depends on the collisional mixing rate in the 2^3P state for single-component OP but also varies with M and W_{abs} for multi-component OP, as is the case for the f_2^- line used at 4.7 T) [24]. The second term accounts for the polarization loss[14]. Just like η, the global polarization loss rate Γ_R introduced in this budget may not be constant. The photon efficiency η is a crucial quantity that must be known (together with the loss rate Γ_R and the absorbed power W_{abs}) to quantitatively derive, predict, or interpret MEOP dynamics [16,24].

Unfortunately η has presently neither been measured nor computed at 4.7 T. However, for this field strength, the build-up rates are observed to be constant and one can combine equations (21) and (25) to obtain:

$$\Gamma_{OP} = 2\,\eta(0) \frac{W_{abs}(0)}{NV_{cell}\hbar\omega_{OP}} \frac{1}{M_{SS}}. \quad (26)$$

At fixed gas density M_{SS} is almost independent of the plasma conditions (Fig. 13a). Γ_{OP} is thus expected to be roughly proportional to $W_{abs}(0)$ if the variations of η remain small (a reasonable assumption since pump power is moderate and absorption is not very high in most cases). This plausibly explains the rough linear increase of Γ_{OP} with n_m^s observed in Figure 13b, at least qualitatively. However, the established link is potentially misleading

[14] The residual loss rate that occurs at $M = 0$ in the presence of OP is neglected [24].

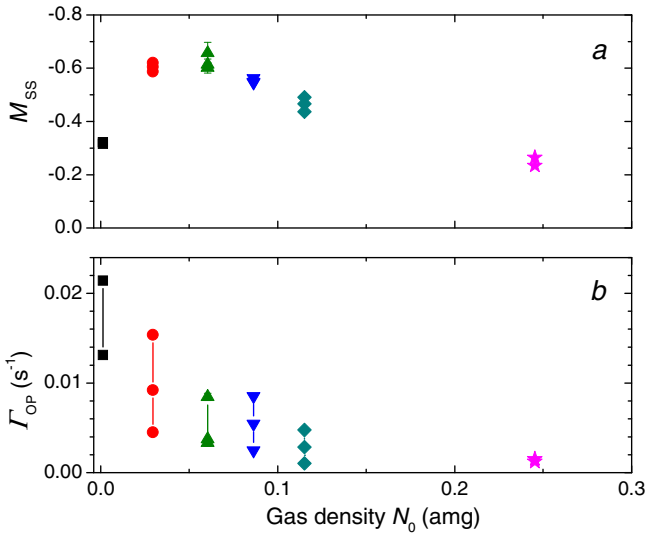

Fig. 14. Density dependence of the steady-state polarization M_{SS} (a) and build-up rate Γ_{OP} (b) obtained at fixed incident power (same data as in Fig. 13: 4.7 T, f_2^- OP line, 0.5 W laser power, various plasma conditions).

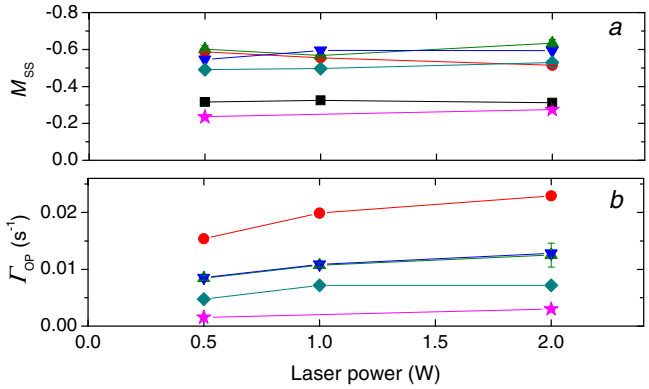

Fig. 15. Variation of the steady-state polarization (a) and build-up rate (b) with incident laser power (4.7 T, f_2^- OP line; same legend as in Fig. 13), at fixed plasma conditions:

p_0 [mbar]	n_m^s [10^{16} m^{-3}]	Γ_D [10^{-3} s^{-1}]	
1.33	12.0	15.4	(±0.3)
32	6.8	2.57	(±0.01)
67	4.5	1.13	(±0.01)
96	5.8	1.92	(±0.01)
128	1.9	1.31	(±0.01)
267	2.0	1.1	(±0.1)

and, in spite of their close relationship, Γ_{OP} is less relevant[15] than $|\dot{M}(0)|$ to analyze the initial growth of M.

The effect of the gas density can be assessed, with the same sets of data, by global comparison of the results obtained in the different cells (Fig. 14). The steady-state polarizations and the build-up rates exhibit markedly different behaviors. Figure 14a shows that $|M_{SS}|$ reaches a broad maximum at moderate density (around 0.6 for $N_0 = 0.03$ and 0.06 amg) and monotonically decreases at high density (to about 0.25 for $N_0 = 0.25$ amg). The rather low polarization ($|M_{SS}| \simeq 0.32$) obtained at low gas density (0.001 amg) may be due to the unfavorable plasma conditions met in the present work (large decay rates Γ_D). The decrease of M_{SS} which occurs at high gas density is systematically observed in MEOP (see Sect. 3.4.2 and Ref. [4]). It may be partly attributed to a global decrease in absorbed OP light power (suggested by the low-power data shown in Fig. 11). However, again, reliable conclusions could only be drawn from direct measurements of both W_{abs} and Γ_R. Figure 14b shows that the polarization build-up rates steadily decrease when N_0 rises, loosing (on average) a factor of twelve between 0.001 and 0.25 amg and reaching $\Gamma_{OP} \simeq 1.4 \times 10^{-3}$ s^{-1} at the highest density (i.e., a pumping time of order 12 min. is achieved at 267 mbar). The density dependence of Γ_{OP} cannot be quantitatively accounted for in a simple way. Based on equation (21), the variation of the build-up rate should result from a strong decrease[16] of $\dot{M}(0)$, mitigated by that of M_{SS}, for increasing N_0. The decrease of M_{SS} is moderate at 4.7 T (Fig. 14a) and $\dot{M}(0)$ is reduced to a smaller extent than expected (see Fig. 16c in Sect. 3.4.1). The interpretation of the results, including the fact that the build-up rates remain constant during OP, would thus require more detailed MEOP investigations.

3.3 Influence of laser power at fixed plasma conditions

The results obtained at fixed rf excitation level for various OP light powers are compiled in Figure 15. Again the behaviors of the steady-state polarization and of the build-up rate are qualitatively different.

The steady-state polarization does not vary much when the OP light power rises from 0.5 to 2 W (Fig. 15a). The relative changes of M_{SS} are small (0.2% on average, with 5% standard deviation) and the scatter of the data is likely due to minor variations in operating conditions. These results are in line with the findings of the high-field studies where measurements have been performed down to much lower laser power (5 mW): at fixed plasma conditions $|M_{SS}|$ rapidly increases with laser power then reaches a smooth plateau, above 0.1−0.2 W in the same cells and with a very similar OP beam (at 32−67 mbar and 0.45–2 T) [13] or above 0.05−0.1 W in 5 cm × 5 cm cylindrical cells with 2-cm-FWHM Gaussian OP beam (at 8−67 mbar and 1.5 T) [5,16]. The data in Figure 15 show that, at 4.7 T as well, above 0.5 W increasing the OP beam power does not yield higher polarizations.

In contrast, the polarization build-up rate increases monotonically with the incident laser power (Fig. 15b). This increase is not linear, as expected. At all gas densities Γ_{OP} is typically only 50% higher when an OP beam with 2 W of light power is used instead of 0.5 W.

[15] $\dot{M}(0)$ is a stand-alone quantity, only determined by W_{abs}. Γ_{OP} additionally depends on M_{SS} (Eq. (26) or (21)), hence on Γ_R.

[16] The OP contribution is expected to be greatly reduced under the joint effect of a decrease of W_{abs} (see Sect. 3.4.1) and of the explicit $1/N_0$ scaling introduced by ME (Eq. (25)).

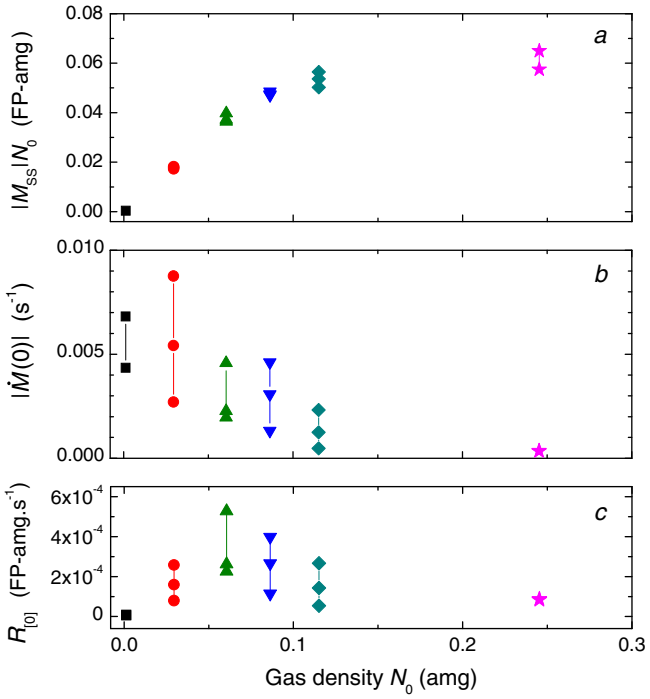

Fig. 16. Variation of the steady-state magnetization $|M_{SS}|N_0$ (a), initial pumping speed $|\dot{M}(0)|$ (b), and magnetization build-up speed $R_{[0]} = |\dot{M}(0)|N_0$ (c) with gas density (4.7 T, f_2^- OP line, 0.5 W laser power; same data as in Fig. 14). FP-amg: magnetization unit corresponding to the magnetization of fully polarized ^{3}He gas ($|M| = 1$) with a number density of 1 amg.

3.4 Discussion

3.4.1 Optimal operating conditions at 4.7 T

In view of applications, the efficiency of MEOP is here globally assessed in terms of magnetization and pumping speed. The analysis is performed with the 0.5 W data reported in Section 3.2 and the results obtained in the different cells, compiled in Figure 16, are compared to determine the potentially best operating conditions at 4.7 T.

The steady-state magnetization (Fig. 16a) increases linearly with N_0 at moderate gas density and levels off around 0.08 amg. Above this value, the rise in density compensates for the decrease in nuclear polarization shown in Figure 14a. At high density M_{SS} is too low to let the ^{3}He sample be a good neutron spin filter or ^{3}He gas target. The polarized gas could still be used for NMR but too much of the rare isotope would be wasted. The same magnetization (hence the same NMR signal) can be achieved with less ^{3}He gas if MEOP is performed at lower density and a buffer gas can be subsequently added to meet the same final pressure or storage conditions (e.g., ^{4}He in the OP cell; ^{4}He or N_2 in the storage cell).

Figure 16b shows that there is no benefit to be expected from operation at very high gas density because pumping speeds are low. Several factors contribute to $\dot{M}(0)$ decrease when N_0 increases. For Dehmelt OP and fixed absorbed pump power, changes in photon efficiency may still occur for the f_2^- line due to a small overlap with the neighboring f_4^- line (see Fig. B.4 in Appendix B.2). More importantly, the collisional line broadening induces a decrease in f_2^- spectral amplitude, hence in pump light absorption (by up to a factor 2, roughly; see Fig. B.5 in Appendix B.2). Furthermore W_{abs} is expected to be reduced by the strong decrease in 2^3S atom density observed in the rf plasmas (Fig. 10). Finally, at $M = 0$ the speed of the OP-driven increase of polarization is inversely proportional to the number of ^{3}He atoms contained in the cell (Eq. (25)). Unsurprisingly, the 0.001 amg data included in Figure 16 are in line with those obtained at higher density. The sub-optimal plasma conditions (about ten times larger decay rates Γ_D) only lead to a faster growth of the ^{3}He polarization towards a smaller steady-state value (Fig. 14).

Figure 16c displays the range of values obtained for the initial magnetization build-up speed. It suggests that operation around 0.06 amg would be the best choice (at least in this type of OP cells) when large throughputs of polarized ^{3}He gas are needed. $R_{[0]}$ can be further improved if more pump light power is used. However, the gain in efficiency is expected to be poor for gas production in the batch mode since there will be no change in M_{SS} and a small increase in Γ_{OP} or $\dot{M}(0)$ in the closed OP volume (see Fig. 15b). The potential gain is more important in the continuous flow mode, which can be straightforwardly established in the simple case where M remains uniform inside the cell. For a constant flow rate Q of ^{3}He atoms, the inlet of unpolarized fresh gas ($M = 0$) and the outlet of optically polarized gas ($M = M_{SS}^Q$) introduce an additional polarization loss rate equal to: $\dot{M}|_{flow} = -M_{SS}^Q \Gamma_{flow}$ with $\Gamma_{flow} = Q/N'V_{cell}$, if N' is the gas density established in steady state. This loss is balanced by the OP speed $\dot{M}|_{OP} = \Gamma_{OP}(M_{SS}^{Q=0} - M_{SS}^Q)$, where Γ_{OP} is the polarization build-up rate and $M_{SS}^{Q=0}$ the steady-state polarization obtained for null flow in the same OP and plasma conditions. The output polarization is thus given by:

$$M_{SS}^Q = \frac{M_{SS}^{Q=0}}{(1 + \Gamma_{flow}/\Gamma_{OP})}. \quad (27)$$

At fixed Γ_{flow} the polarization extracted from the OP cell will be higher for a larger build-up rate Γ_{OP}, i.e., for a more intense pumping beam. Of course the saturation of the build-up rate at high laser power (Fig. 15b) ultimately sets a limit to the manageable flow rates. Larger amounts of polarized gas can then be produced only if the OP cell volume is increased. When large OP cells are used[17] the diffusion time along the cell axis exceeds $1/\Gamma_{flow}$ and M no longer remains uniform in this direction. OP being faster at the entrance than at the exit of the cell, the average pumping speed is larger and equation (27) only provides a lower bound for M_{SS}^Q. The output polarization actually achieved in steady state under flow can nevertheless be numerically computed, with the parameters of MEOP dynamics experimentally measured for closed OP volumes.

[17] In practice several long cells with optimal diameters are used and optically pumped in parallel to maximize the volume flow and output polarization of the production unit [6,33].

This task is simple to carry out at 4.7 T because the build-up rate Γ_{OP} is independent of M.

3.4.2 Optimal magnetic field strength

In the 0.03−0.25 amg range, the decay rates measured at 4.7 T are quite similar to those obtained in the same cells at 1.5–2 T [13] or in 5 cm×5 cm cells at 1.5 T [5]. The correlation between Γ_D and n_m^s (Fig. 10a) is also reminiscent of that observed, in a variety of MEOP cells, down to a few milliteslas. Altogether there is no major difference in plasma conditions with previous high-field studies and the results can be globally compared. In contrast, it should be noted that weaker discharges could be sustained in the bone-shaped 0.001 amg cell at 1.5 T (yielding both longer decay times, $1/\Gamma_D = 50-800$ s, and lower 2^3S atom densities, $n_m^s = 0.2–5 \times 10^{16}$ m^{-3}) [34]. More favorable MEOP conditions have also been obtained in a 5 cm×5 cm cell with identical gas density ($1/\Gamma_D = 300–1000$ s and $n_m^s = 0.4–2.5 \times 10^{16}$ m^{-3}), yielding polarizations up to $M_{SS} = -0.80$ [5]. The 0.001 amg data are thus excluded from the present discussion.

For all other field strengths investigated to date the approach to the steady-state value of the polarization is not exponential. A time dependent build-up rate $\Gamma(t)$ is often introduced, defined by:

$$\dot{M}(t) = \Gamma(t)(M_{SS} - M(t)) \quad (28)$$

if OP starts at $t = 0$ from $M = 0$. Γ typically decreases by up to 50% at high polarization [3,14,16,20,24,32] and MEOP results for $B \leq 2$ T have actually been reported in terms of M_{SS} and τ_b, where τ_b is the inverse of the rate measured at $M = 0$. The quantity $\Gamma(0) = 1/\tau_b = \dot{M}(0)/M_{SS}$ can thus be directly compared to the constant build-up rate Γ_{OP} measured at 4.7 T. Selected results from reference [13], obtained in the 0.03 and 0.06 amg cells for f_2^- OP, are replotted in Figure 17. These measurements have been performed in the so-called "weak discharge" conditions, with 0.5 W of laser power and a Gaussian OP beam (3 mm FWHM) that was delivered by a monochromatic 1083 nm laser source. The narrower spectral bandwidth (a few MHz) is however expected to have a limited adverse impact on MEOP efficiency, thanks to the strong collisional mixing between velocity classes in this pressure range [24]. Three graphs allow a comparison to the matching 4.7 T results (Figs. 14 and 16 data) which, for clarity, are represented by their average values and spans over the investigated ranges of plasma conditions.

In Figure 17a, following a nearly linear increase of M_{SS} with the magnetic field strength up to 1.5 T, the data seem to level off and the same polarization value is obtained at 2 and 4.7 T ($M_{SS} \simeq -0.60$). The observed change in behavior suggests that the competition between OP and relaxation processes in the rf plasmas leads to a different balance above 2 T. This remains to be explained since neither the photon efficiency nor the OP contribution to the angular momentum budget are expected to change drastically in this field range.

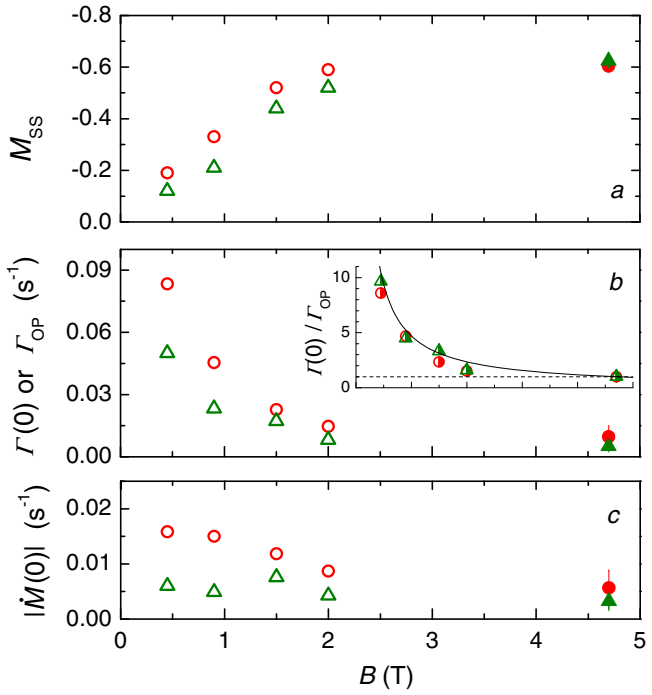

Fig. 17. Comparison of MEOP results at 4.7 T (this work; solid symbols: average values in the rf plasmas, bars: spans) and at lower field ($B = 0.45–2$ T, Tab. 2 in Ref. [13]; open symbols) for moderate density (0.03 amg: red circles, 0.06 amg: green up triangles). (a) Steady-state polarization M_{SS}. (b) Build-up rates Γ_{OP} (constant value, 4.7 T) and $\Gamma(0)$ (initial value, [13]; see Eq. (28)). Inset: Data set ratio $\Gamma(0)/\Gamma_{OP}$ (semi-filled symbols, same shapes and colors). Solid line: $4.7/B[T]$, a guide for the eye. (c) Initial pumping speed $|\dot{M}(0)|$ (for all data: f_2^- OP line, 0.5 W light power; plasma conditions: see the list below).

	n_m^s (10^{16}m^{-3})	Γ_D (10^{-3}s^{-1})	n_m^s (10^{16}m^{-3})	Γ_D (10^{-3}s^{-1})
32 mbar	3.5−6.8	0.4−2.5	2.9−5.9	1.2−1.8
67 mbar	2.4−4.5	0.7−1.1	1.5−6.8	0.8−1.3
	$B = 4.7$ T		$B = 0.45–2$ T [13]	

Figure 17b shows that, as expected, the initial polarization build-up rate steadily decreases up to 4.7 T at fixed gas density. Because of hyperfine decoupling, less nuclear orientation is transferred by each ME collision and a larger number of binary interactions are required to transfer the same amount of angular momentum [5,15]. One can also argue that, since the coupling to the ground state reservoir introduced by ME is less efficient at high field, the OP light induces a larger skew of the distribution of populations in the 2^3S state [23,24]. This reduces the absorbed laser power and, hence, the initial build-up rate at fixed plasma conditions (Eq. (25)). The relative variations of $\Gamma(0)$ with B are comparable in the two cells (Fig. 17b, inset) within the experimental data scatter, mainly due to differences in 2^3S atom density. The build-up rates measured at $M = 0$ are typically ten times higher at 0.45 T than at 4.7 T for the selected data. The limited number and quality of the data, combined with the significant differences in operating conditions, does not permit a reliable

fit to this large field dependence. A detailed computation of the impact of hyperfine decoupling on OP dynamics would require a quantitative assessment of the 2^3S state populations in the presence of the pump beam. More extensive investigations, with accurate measurements of the absorbed pump power and of the polarization loss rate, would also be needed to validate beforehand a predictive high-field MEOP model.

Figure 17c shows the variation of the pumping speeds measured at $M = 0$. They globally decrease when B increases but in more progressive way than the build-up rates, thanks to the rise of the nuclear polarization values. They are systematically lower at 0.06 amg and exhibit a smaller decrease at high B. As a result for $R_{[0]}$ a cross-over occurs around 1.5 T, due to the gain in ^{3}He density, and above this value operation at 0.06 amg becomes slightly more efficient in terms of magnetization build-up speed.

The investigations of MEOP at 1.5 and 2 T described in reference [13] have been repeated at 0.03 and 0.06 amg with a broadband 1083 nm fiber laser similar to that described in Section 2.1. They have also been extended to higher ^{3}He density with the bone-shaped cells used at 4.7 T [17,20,34]. Selected (unpublished) results from reference [20], obtained at 2 T with a Gaussian OP beam profile, are presented in Figure 18. The data in Figure 18a confirm that similar values of steady-state polarization are obtained at moderate gas density for both field strengths. More importantly, they show that at high density significantly higher M_{SS} can be achieved at 4.7 T. The ratio between the average values obtained at 4.7 and 2 T rises fairly linearly with N_0, increasing nearly by a factor two from 0.03 to 0.25 amg (Fig. 18a, inset). Conversely, the data in Figure 18b show that the polarization build-up rates are notably smaller at 4.7 T for all gas densities. On average the ratio $\Gamma_{OP}/\Gamma(0)$ decreases linearly when N_0 rises, roughly varying by a factor 1.8 over the same range (Fig. 18b, inset; the scatter of the data is larger since different and wider ranges of 2^3S atom density are probed in Ref. [20]). As a result, the relative loss in pumping speed due to operation at 4.7 T rather than at 2 T is fairly independent of the gas density (Fig. 18c) and MEOP is globally three times slower at 4.7 T.

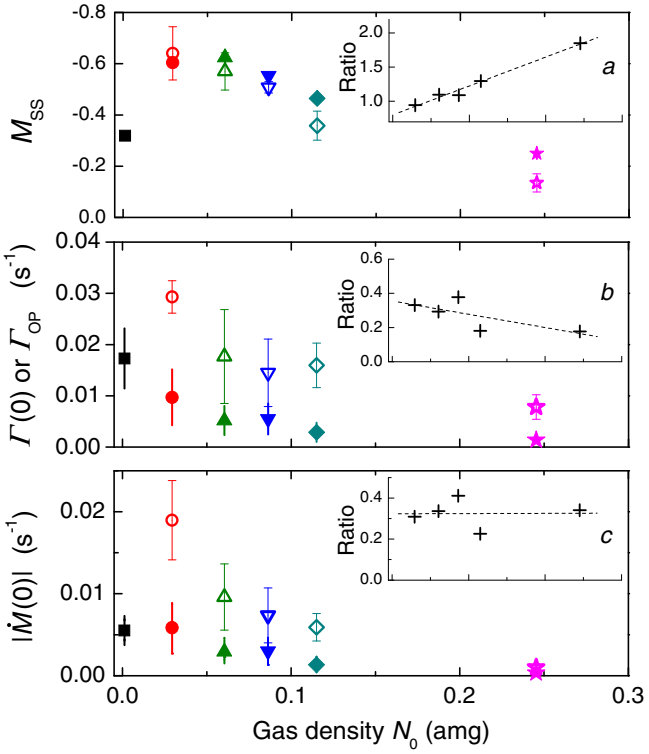

Fig. 18. Comparison of MEOP results at 4.7 T (Fig. 14 data, solid symbols) and 2 T ([20], open symbols). Symbols: mean values, bars: spans). (a) Steady-state polarization. (b) Initial build-up rate (Γ_{OP}, constant value at 4.7 T, $\Gamma(0) = 1/\tau_b$ at 2 T [20]). (c) Initial pumping speed. Insets: data set ratio (4.7 T ÷ 2 T values), same N_0 axis (f_2^- OP line, 0.5 W laser power; plasma conditions: see Figs. 9 and 10 for 4.7 T and the list below for 2 T).

p_0 (mbar)	n_m^s (10^{16}m^{-3})	Γ_D (10^{-3}s^{-1})
32	9.8–20.4	1.3–2.8
67	2.6–12.1	0.6–2.3
96	2.9–9.4	1.3–3.9
128	5.4–9.8	2.5–8.5
267	2.0–3.4	3.5–5.9

4 Conclusion

The experimental results reported in Sections 3.2 to 3.4 provide lower bounds for the efficiency of MEOP at 4.7 T. A choice has been made to use the same glass cells at all field strengths for an investigation of high-field MEOP in comparable conditions. Plasma or OP conditions remain to be fully optimized for operation at 4.7 T. The goal of this study was to extend the range of gas density and field strength investigated in reference [13] and, hereby, to probe a larger portion of the parameter space searched for the best operating conditions for MEOP in pure ^{3}He gas. For filling pressures increasing from 64 to 267 mbar a significant decrease of the steady-state nuclear polarization is demonstrated at 4.7 T, similar to (but weaker than) that subsequently measured at 2 T in the same series of high-pressure cells. As a result, the net increase in magnetization density that is still obtained (thanks to the linear increase in gas density) is larger at 4.7 T, yielding, to the authors' best knowledge, the highest values ever achieved by metastability exchange optical pumping before gas compression. This makes high-field MEOP particularly attractive for magnetic resonance imaging of the lungs. Operation well above millibar pressures in the OP cell puts less demanding requirements for compression stages in the MEOP-based gas polarization systems. This greatly facilitates the production of hyperpolarized ^{3}He for all applications that do not require record high nuclear polarization.

In spite of the limited duration of the experimental investigation carried out at 4.7 T, a consistent body of data has been obtained using the f_2^- OP line which allows direct comparison with previous high-field studies. A number of

complementary measurements could be performed for an exhaustive investigation of MEOP and of the underlying physics. For instance, other lines may be used for OP. A few exploratory tests have been performed at 4.7 T with the f_2^+ line in some of the ^{3}He cells. Similar polarizations and build-up rates have been obtained. Based on the 1.5 T and 2 T results of references [13,23], lower polarization but faster build-up may be expected using the stronger f_4^- line for OP, which may be an advantage when large throughputs are needed for gas production. However, this OP line includes four components with different or opposite photon efficiencies and the influence of pump laser linewidth and tuning must be carefully investigated (at all gas densities since collisional broadening is expected to affect the global impact of multi-component excitation). The few single-component resolved lines present in the high-field spectrum of the 2^3S-2^3P transition of ^{3}He are weak and, hence, of little interest for efficient production of polarized gas. However, their photon efficiencies are independent of the ^{3}He nuclear polarization and, provided that the amount of OP light power absorbed by the gas is accurately measured, they can be used for experimental studies of the laser-enhanced relaxation and for straightforward quantitative comparison with the predictions of available MEOP models [14,24].

The methodology developed for the 4.7 T study benefits from the recent improvement in understanding and modeling of MEOP that has been triggered by very detailed investigations performed at low field and high laser power [14]. Accurate results obtained over an extended range of field strengths and gas densities will hopefully allow to discriminate between physical processes potentially involved in laser-enhanced relaxation [24] and help in finding a way to push even further the limits to MEOP efficiency. So far high-field MEOP has been investigated only in pure ^{3}He gas. The study could also be extended to isotopic He mixtures where one might advantageously capitalize on the more efficient light absorption by ^{4}He atoms to obtain larger build-up rates and higher nuclear polarizations, as demonstrated at low magnetic field [35,36]. The potential gain in efficiency would be of interest for all applications where dilution of ^{3}He in ^{4}He does not cause any problem, as is the case for neutron spin polarization or polarimetry, as well as for MRI, for instance.

Such detailed fundamental studies fall beyond the scope of the present work, whose primary objective was a pragmatic identification of the best operating conditions for ^{3}He MEOP in view of its applications. The collected data clearly show that operation at 4.7 T is a good option only if OP must be directly performed at very high gas density and if the longer polarization build-up times are not an issue. Otherwise, operation at 1.5 T or 2 T has two major advantages. First, such field strengths are more commonly available and provided by a majority of clinical MRI scanners. Second, higher build-up rates are achieved by MEOP and the steady-state polarizations obtained at moderate gas densities are still high. In any case, it is likely that the results reported in this article can be further improved by dedicated optimization of the plasma conditions or of the cell geometry and laser beam profiles. For instance, conical lenses (axicons) have recently been used to reshape the OP beam and to obtain an annular transverse distribution of light intensity that better matches the radial distributions of 2^3S atoms in the high-pressure cells, demonstrating that MEOP efficiency can be successfully increased [17,20,34]. High-field MEOP has recently been implemented for on-line gas production inside a clinical scanner with a prototype polarizer designed to optimally combine the current experimental findings [34,37].

Financing support from the European network PHeLINet (MRTN-CT-2006-36002) and the Polish Ministry of Science and Higher Education (SPUB 547/6.PRUE/2008/07) is gratefully acknowledged. Glass work has been carried out at L.K.B. in Paris by Florence Thibout. Access to the 4.7 T magnet has been kindly granted by the MRI department of the Inst. of Nucl. Phys. in Krakow.

Appendix A: Modulation depth of absorption signals

If, driven by the modulated applied rf voltage, the number density of metastable 2^3S atoms in the plasma n_m is assumed to oscillate at low angular frequency ω_D around some average value n_m^0 with a relative amplitude ϵ:

$$n_\mathrm{m}(t) = n_\mathrm{m}^0(1 + \epsilon \sin \omega_\mathrm{D} t), \tag{A.1}$$

the probe light power transmitted through the cell at time t is equal to: $\mathcal{P}_\mathrm{on}(t) = \mathcal{P}_\mathrm{off} \exp\{-\beta^0\} \exp\{-\epsilon\beta^0 \sin \omega_\mathrm{D} t\}$ ($\mathcal{P}_\mathrm{off}$: power transmitted without rf discharge; β^0: plasma absorbance for the average density of absorbers n_m^0). The photodiode PD2 thus provides in the detection channel a signal with an average component V:

$$V = V_\mathrm{off} \exp\{-\beta^0\} \left\langle \exp\{-\epsilon\beta^0 \sin \omega_\mathrm{D} t\} \right\rangle \tag{A.2}$$

and a demodulated component r:

$$r = V_\mathrm{off} \exp\{-\beta^0\} \left\langle \sin \omega_\mathrm{D} t \exp\{-\epsilon\beta^0 \sin \omega_\mathrm{D} t\} \right\rangle \tag{A.3}$$

where V_off is the average value obtained without discharge. The expressions with angle brackets stand for the time-averaged values of their arguments over the period $2\pi/\omega_\mathrm{D}$.

The ratio between the demodulated and average components is independent of the power of the probe light beam, hence immune to its fluctuations. A Taylor expansion yields, for small values of the product $\epsilon\beta^0$:

$$\frac{r}{V} = -\frac{\epsilon\beta^0}{2} + \frac{(\epsilon\beta^0)^3}{16} + \cdots \tag{A.4}$$

which shows that, to first order, the signal modulation depth is proportional to the average light absorbance. The exact expression of r/V can be computed using the modified Bessel functions of the first kind of order 0 and 1, I_0 and I_1 (respectively):

$$\frac{r}{V} = -\frac{I_1(\epsilon\beta^0)}{I_0(\epsilon\beta^0)}, \tag{A.5}$$

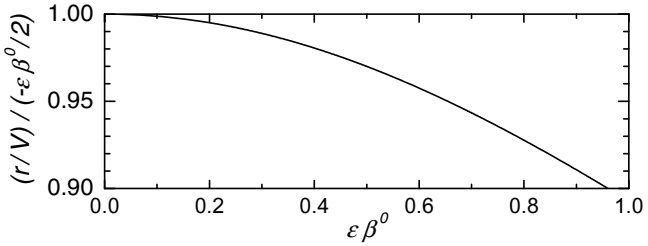

Fig. A.1. Computed ratio between the exact value of r/V (Eq. (A.5)) and its first-order approximation $(-\epsilon\beta^0/2)$, plotted for $0 \leq \epsilon\beta^0 \leq 1$.

since for integer value n the integral formula of I_n is: $I_n(z) = (1/\pi)\int_0^\pi \exp[z\cos\theta]\cos(n\theta)d\theta$.

Figure A.1 allows a quantitative comparison between the exact and first-order values of r/V for small amplitudes of discharge modulation. The linear approximation remains valid for fairly large ϵ when absorbance is small. This occurs for the measurements performed with the weak σ^+ line doublet and makes the modulation technique particularly useful for sensitive detection of small changes in 1083 nm light absorption by the plasma.

Appendix B: 2^3S-2^3P line shape adjustments

B.1 Fitting procedure

The computer program used for data processing averages the absorption signals from the probe line doublet scans recorded at $M = 0$ before OP and provides a set of experimental transmittance data D_n for the $N^{\rm SF}$ sampled frequencies ($N^{\rm SF} \simeq 500$). For a fixed temperature $T_{\rm gas}$ and Lorentzian FHWM values $\overline{\omega}_{\rm L}$ ranging from 0.2 to 4 GHz, series of $N^{\rm SF}$ spectral amplitudes S_n^+ are computed for $a_i = 1/6$ using equations (8) and (5), with the 22 σ^+ components of the 2^3S-2^3P transition at 4.7 T [15]. The fitting program adjusts the vertical and horizontal scales for the experimental data so as to minimize the error function $E = \sqrt{\sum_n (D_n - S_n^+)^2/(N^{\rm SF}-1)}$ (standard deviation of the residua). A downhill simplex method is used for the minimization [38].

Figure B.1 shows an example of experimental data set and adjustments. The quality of each adjustment cannot be determined with the χ^2 test because the distribution for the random deviations of the experimental data is not known. Instead, the estimation of the uncertainty is based on the observed sensitivity of the error to variations of $\overline{\omega}_{\rm L}$ (Fig. B.2). Using a parabolic fit of $E(\overline{\omega}_{\rm L})$ the best adjusted value is obtained for $\overline{\omega}_{\rm L}$ and the error bar $\delta\overline{\omega}_{\rm L}$ is chosen so as to yield an error equal to twice the minimum value of E. As shown in Figure B.2, at 0.25 amg several input temperatures yield comparable minimum errors.

The adjustment of $T_{\rm gas}$ is not straightforward in the investigated range of gas density, where $\overline{\omega}_{\rm L}$ and $\overline{\omega}_{\rm G}$ are comparable in magnitude and have a qualitatively distinct impact on S^+ (Fig. B.3). Figure B.3a shows the spectrum computed with the best fit FWHM values obtained

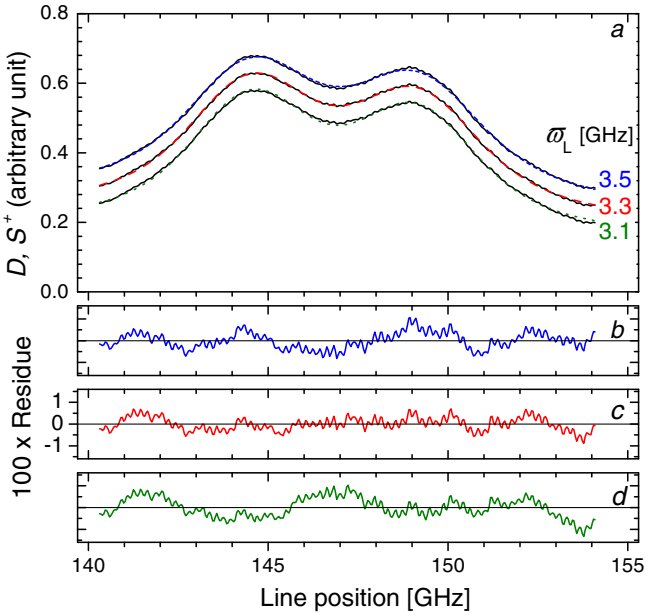

Fig. B.1. Example of adjustments for one recording. (a) Scaled data (D; black lines) and spectral amplitudes computed for $T_{\rm gas} = 350$ K and various $\overline{\omega}_{\rm L}$ (S^+; from top to bottom: 3.5, 3.3, and 3.1 GHz (blue, red, and green dotted lines, see legend)). The graphs are shifted for clarity and the residua are plotted in the lower panels: (b), (c) (best fit), and (d), resp. (identical magnified scale, matched line colors) (exp. conditions: 4.7 T; 0.25 amg; $M = 0$; $n_{\rm m}^{\rm s} = 5.8 \times 10^{16}{\rm m}^{-3}$, $\Gamma_{\rm D} = (1.92 \pm 0.01) \times 10^{-3}$ s^{-1}).

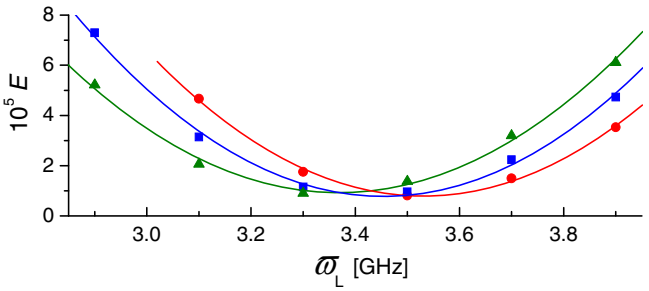

Fig. B.2. Example of errors E (symbols) and parabolic fits (lines) obtained for various $T_{\rm gas}$ by adjustments to the experimental data of Figure B.1. Red dots: 300 K; blue squares: 325 K; green triangles: 350 K.

at 0.25 amg (Tab. B.1, Appendix B.2) and those obtained for a 10% lower $T_{\rm gas}$ or $\overline{\omega}_{\rm L}$ value. The decrease of $T_{\rm gas}$ induces a fairly uniform relative variation (about −5%, Fig. B.3b) and a broad absolute decrease of S^+ which reaches its maximum at the center of the doublet spectrum (Fig. B.3c). The decrease of $\overline{\omega}_{\rm L}$ yields, of course, a larger relative change in the outer wings (about −9%) and a smaller one in the central part. The peaks heights, as well as the dip between the two lines are enhanced. These differences in behavior explain the significantly lower sensitivity of the adjustments to the parameter $T_{\rm gas}$, because the experimental data include a global scaling factor associated with the average 2^3S atom density $n_{\rm m}^{\rm s}$

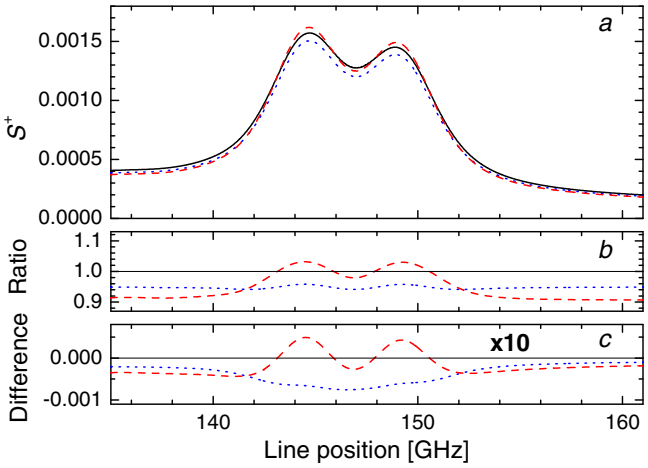

Fig. B.3. Influence of T_{gas} and $\overline{\omega}_L$ at 0.25 amg. (a) Spectral amplitudes computed with Table B.1 best fit values (350 K, 3.3 GHz; solid black line, reference data for the lower panels), with a lower T_{gas} (315 K, blue dot; $\overline{\omega}_G$ is thus 5.2% lower), or lower $\overline{\omega}_L$ (3.0 GHz, red dash). The ratio (b) and difference (c), (amplified by a factor 10) in S^+ values (same line styles and colors) show the distinct impact of the two input parameters.

and its (unknown) modulation amplitude driven by the rf excitation.

For each OP cell, line shape adjustments are performed for all the recordings (MEOP measurements for three rf levels, one test of reproducibility). The data are sometimes too noisy to provide helpful discrimination between adjusted $\overline{\omega}_L$ values. However, on average, the uncertainty $\delta\overline{\omega}_L$ ranges from ±0.1 to ±0.2 GHz for the individual recordings and the results are consistent within $\delta T_{gas} \simeq \pm 10$ K for the whole run (with an individual uncertainty on T_{gas} culminating at ±20 K at high density).

B.2 Experimental results and discussion

Using the method described in Appendix B.3, the raw adjusted values are individually scaled in temperature for global compilation and linear fit at 300 K (Sect. 2.4.2). This compilation provides a check of consistency for all line shape adjustments. It is also used to infer a single optimal Lorentzian FWHM for each cell. This optimal FWHM $\overline{\omega}_L$ is computed from the $\overline{\omega}'_L$ value provided by the linear fit (Fig. 6) using the average value of T_{gas} for back-scaling to the operating temperature.

Table B.1 provides the final results of the line shape adjustments performed at 4.7 T. It lists the pairs of best fit parameters T_{gas} and $\overline{\omega}_L$ that are used in the data reduction process for computation of all spectral amplitudes. In the 0.001 amg cell the analysis of the spectra yields $T_{gas} = 300$ K but SNR is too low to allow reliable adjustments of $\overline{\omega}_L$. The FWHM value which appears in brackets in Table B.1 is inferred by linear extrapolation of the results obtained in the other cells. The cell contents are also listed in Table B.1. The filling pressure p_0 (±0.001 mbar at 1.33 mbar, ±0.13 mbar at 267 mbar, and ±0.01 mbar

Table B.1. Best-fit values of T_{gas} (average gas temperature) and $\overline{\omega}_L$ (optimal Lorentzian FWHM) obtained by adjustments of the σ^+ probe doublet spectra recorded at 4.7 T for $M = 0$. The Gaussian FWHM $\overline{\omega}_G$ is inferred from T_{gas} (Eq. (7)) and the ^{3}He gas density (N_0) from the cell filling pressure (p_0) and filling temperature (T_0). Accuracy is specified in the text.

N_0 (amg)	T_{gas} (K)	$\overline{\omega}_G$ (GHz)	$\overline{\omega}_L$ (GHz)	p_0 (mbar)	T_0 (°C)
$1.215\ 10^{-3}$	300	1.978	[0.027]	1.331	22.0
$2.941\ 10^{-2}$	300	1.978	0.38	32.40	23.8
$6.047\ 10^{-2}$	325	2.059	0.81	66.77	24.5
$8.634\ 10^{-2}$	325	2.059	1.16	96.33	27.6
0.1152	325	2.059	1.55	128.43	27.6
0.2454	350	2.137	3.31	267.18	20.4

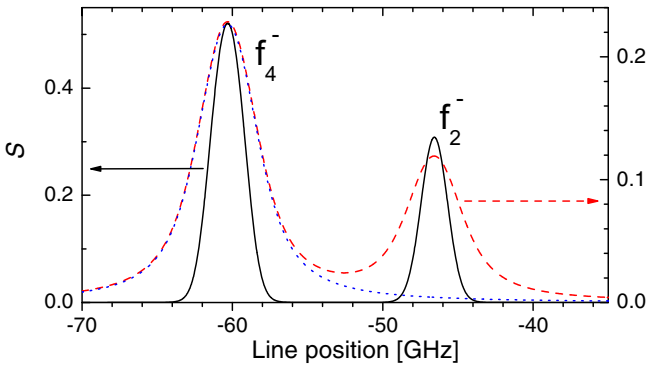

Fig. B.4. Impact of collisional broadening on f_2^- line shape at 4.7 T. Spectral amplitudes are computed at $M = 0$ for σ^- light using Table B.1 values for 0.001 amg (solid black line, left scale) and 0.25 amg (red dash, right scale; the f_4^- line (blue dot) contributes 3.4% to the f_2^- peak height).

otherwise) and filling temperature T_0 (±0.1 °C) are used to compute the ^{3}He number density N_0. The amagat is the ideal gas number density at 101.325 kPa and 273.15 K (1 amg = 2.6868×10^{25} m^{-3}).

Collisional broadening provides the leading contribution to the differences in Voigt line shape observed in the OP cells. It has an impact on the weak probe lines used for detection (discussed in Sect. 2.4.1 and illustrated in Fig. 5) but also on the strong f_2^- line used for OP (Fig. B.4). At the highest density (0.25 amg: $T_{gas} = 350$ K, $\overline{\omega}_L = 3.31$ GHz) the peak height is substantially reduced ($S = 0.119$, versus 0.308 at 0.001 amg), hence less OP light is absorbed at fixed n_m^s. Moreover the f_2^- line is no longer fully resolved and S includes a small contribution (0.004) from the neighboring f_4^- line which potentially affects the photon efficiency.

The evolution of the peak amplitude with the gas density is shown in Figure B.5 for the OP and probe lines, at $M = 0$. The decrease of S with N_0 is mildly slower for the probe doublet (solid symbols in Fig. B.5), due to the increasing contribution of the neighboring σ^+ strong lines (slanted baseline, see Sect. 2.4.1). The small difference in behavior between A_2-B_9 and A_1-B_{10} arises from the difference in position and from the progressive overlap of the two probe lines. Table B.2 lists the corresponding

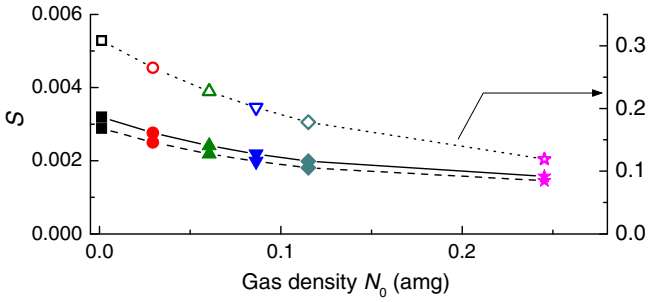

Fig. B.5. Computed peak spectral amplitudes of the σ^+ probe lines (left scale, solid symbols with solid (A_2-B_9) and dashed (A_1-B_{10}) connecting lines) and f_2^- OP line (right scale, open symbols and dotted line) at 4.7T, obtained for $M = 0$ with Table B.1 best-fit FWHM values.

Table B.2. Peak spectral amplitudes of the A_1-B_{10} and A_2-B_9 probe lines ($S_1^+(0)$ and $S_2^+(0)$, resp.; see Eq. (16)) computed at 4.7 T for $M = 0$ with Table B.1 FWHM values.

MEOP cell		Peak amplitudes	
N_0 (amg)	p_0 (mbar)	$S_1^+(0)$	$S_2^+(0)$
0.0012	1.3	0.00288	0.00319
0.029	32	0.00250	0.00276
0.061	67	0.00219	0.00241
0.086	96	0.00198	0.00218
0.115	128	0.00181	0.00199
0.245	267	0.00145	0.00157

peak values, which are used for the absolute measurements of n_m^s (Sect. 2.4.4). From an experimental point of view, broader atomic lines yield lower SNR for the absorption-based measurements. For instance, if the operating conditions are compared at 0.03 and 0.25 amg, the reduced spectral amplitude (average S ratio 1:1.74) combined with the lower range of 2^3S atom densities (n_m^s ratios 1:2.1−1:6.5 in Fig. 10) leads to a substantial decrease of the magnitude of the optical signals.

B.3 Temperature scaling law for $\overline{\omega}_L$

The data scaling method is based on the known temperature dependence of the gas pressure p inside the OP cell and on the expected temperature dependence of the cross section for collisional mixing derived from published numerical data. Ab initio calculations of the collisional broadening and shift of the 2^3S-2^3P transition are performed for ^{4}He in reference [29] and, for clarity, the original notations are used in this paragraph. The broadening width w (half width at half maximum, HWHM) and shift d considered for collisions of (minority) excited atoms with (majority) ground state atoms are defined by $w - id = \hbar N \langle v\sigma_{\alpha\beta}\rangle$ for initial and final radiative states α and β. Consequently the pressure broadening rate w/p is computed for the (ideal) ^{4}He gas at thermal equilibrium as:

$$w/p = \hbar \frac{\langle v\rangle}{k_B T} \Re e \langle \sigma_{\alpha\beta}\rangle .$$

In this expression (Eq. (4) of Ref. [29]) $\langle v\rangle = \sqrt{8k_BT/\pi\mu}$ is the average velocity and $\langle\sigma_{\alpha\beta}\rangle$ is the energy average cross section ($\hbar$ and k_B: usual fundamental constants, μ: reduced mass). Numerical values are provided for the three components of the 1083 nm transition of ^{4}He, 2^3S-2^3P$_J$ ($J = 0, 1, 2$), in Table II of reference [29]. The temperature dependence of the cross section for collisional mixing is inferred from non-linear adjustments of these published data, according to:

$$w/p = w^0 (T^K/300)^\zeta,$$

where T^K is the value of temperature T in Kelvin. For the three sets of computed data the selected fit function yield good adjustments, with similar relative standard deviations ($\delta w^0/w^0 = 5 \times 10^{-4}$ and $\delta\zeta/\zeta = 3.6 \times 10^{-4}$). A combination of these adjustments provides the following average fit parameters: $w^0 = 12.0344 \pm 0.0120$ MHz/Torr, $\zeta = -0.6465 \pm 7 \times 10^{-4}$.

In the 4.7 T experiment, the line shape measurements that yield the adjusted values of T_{gas} and $\overline{\omega}_L$ are performed at constant ^{3}He gas density N_0 in the sealed glass cells. The collisional FWHM is thus expected to satisfy:

$$\overline{\omega}_L = 2N_0\hbar \langle v\rangle \Re e \langle\sigma_{\alpha\beta}\rangle \propto N_0 T^{1+\zeta} = N_0 T^\xi, \quad \text{(B.1)}$$

and a comparison of the data obtained in the various cells can be made at fixed temperature $T = 300$ K using:

$$\overline{\omega}'_L = \overline{\omega}_L (300/T^K_{gas})^\xi \quad \text{(B.2)}$$

$$\text{with } \xi = 1 + \zeta = 0.3535 \pm 0.0007. \quad \text{(B.3)}$$

This direct scaling legitimately neglects the residual Lorentzian FHWM at null pressure, small compared to the adjustment error bars, that results from the atomic natural width and the probe laser linewidth (see Sect. 2.4.2).

The experimental broadening rate at 300 K reported in the text ($\overline{\omega}'_L/p$, Sect. 2.4.2) is obtained by a linear fit of the scaled FWHM data $\overline{\omega}'_L$ plotted against gas pressure p at 300 K (Fig. 6). The pressure is obtained from the cell filling pressure p_0 using $p = p_0(300/T_0^K)$, where T_0^K is the value of the cell filling temperature in Kelvin.

Appendix C: 1083 nm light absorption measurements

Appendix C.1 provides the general background for the absorption-based measurements of the ^{3}He polarization M and of the 2^3S atom density n_m performed with the probe beam (see Sect. 2.4). The two issues raised by those performed with the attenuated OP beam are subsequently addressed: excitation with broadband light (Appendix C.2) or with a wide laser beam (Appendix C.3). Finally, the limited applicability of absorption-based optical detection in the presence of OP is briefly discussed (Appendix C.4).

Light absorption is probed at 1083 nm with low power and circular polarization ($e_\lambda = e_+$ and e_- for the probe and pump beam, respectively). Inside the cylindrical OP cell, schematically depicted in Figure C.1, the value of

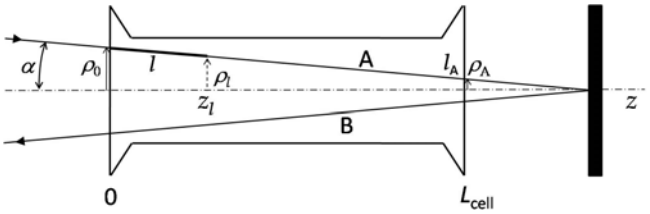

Fig. C.1. Sketch of the OP cell (not to scale). The cell axis defines the horizontal axis of symmetry z, common to the Cartesian (O,x,y,z) and cylindrical (O,ρ,ϑ,z) coordinate systems. ρ_0 and ρ_A: radial positions of entrance and exit points (resp.) for light path A. Along this segment, the linear abscissa l corresponds to the cylindrical coordinates $z_l = l\cos\alpha$ and $\rho_l = \rho_0 - l\sin\alpha = \rho_0 - l(\rho_0-\rho_A)/l_A$.

n_m at point $\overrightarrow{r}(x,y,z)$ is assumed to depend only on the distance to the axis, $\rho = \sqrt{x^2+y^2}$. The probe path includes the linear segments A and B, with identical length l_A and tilt angle α, for which the light absorbances are equal by symmetry (total path length: $L_{path} = 2l_A\cos\alpha \approx 2L_{cell}$)[18]. The pump path is parallel to the axis ($L_{path} = 2L_{cell}$). The following computations are performed in the linear absorption regime (relevant for all experiments) where the loss at point $\overrightarrow{r}$ is proportional to the local values of the intensity $\mathcal{I}(\overrightarrow{r})$ and of the density of absorbers $n_m(\overrightarrow{r})$.

C.1 Monochromatic light absorption measured with a narrow probe beam: optical detection at 1083 nm

The diaphragmed laser beam (single frequency $\nu = \nu_{\mathcal{L}}$) being designed to probe absorption along the 1D paths A and B only, the equation of propagation is derived from the computation of the local loss of light intensity:

$$\frac{d\mathcal{I}}{dl} = -n_m(l)\sigma(\nu_{\mathcal{L}},e_\lambda)\mathcal{I}(l), \tag{C.1}$$

where $\sigma(\nu,e_\lambda) = \widetilde{\sigma}S(\nu,e_\lambda)$ is the cross section for monochromatic light absorption (see text, Sect. 2.4.1). Equation (C.1) explicitly assumes that the cross section σ is uniform inside the cell. This is true in the absence of OP (or with OP when ME dominates) since the populations a_i are in spin-temperature equilibrium with the (uniform) nuclear polarization M. It is generally not true when some OP light strongly excites the atoms and locally perturbs the distribution of atoms among sublevels in the 2^3S and 2^3P states. Equation (C.1) leads to the well known exponential decrease of the light intensity (Beer-Lambert law):

$$\mathcal{I}(l) = \mathcal{I}(0)\exp\left\{-\widetilde{\sigma}S(\nu_{\mathcal{L}},e_\lambda)\int_0^l n_m(l')dl'\right\}. \tag{C.2}$$

[18] The losses introduced by the cell windows (and by the back-reflecting mirror for the 2nd pass) introduce a global attenuation factor that cancels out in the ratio of transmitted powers. Weak multiple reflections and interferences inside the cell are neglected.

For segment A $\mathcal{P}(l_A)/\mathcal{P}(0) = \mathcal{I}(l_A)/\mathcal{I}(0)$ and the absorbance is equal to: $l_A n_m^s \widetilde{\sigma}S(\nu_{\mathcal{L}},e_\lambda)$, where n_m^s is the 1D average of the 2^3S atom density sampled along the straight path: $n_m^s = l_A^{-1}\int_0^{l_A} n_m(l')dl'$. The tilt of this path simply provides an average value of the transverse distribution of n_m over the probed fraction of the cell radius:

$$n_m^s = (\rho_0-\rho_A)^{-1}\int_{\rho_0}^{\rho_A} n_m(\rho)d\rho, \tag{C.3}$$

whereas a path parallel to the cell axis ($\alpha = 0$) would just yield $n_m(\rho_0)$. The light absorbance is two times larger for the V-shaped path used in the experiments and equal to:

$$-\ln\mathcal{T}_{mono} = L_{path}n_m^s\widetilde{\sigma}S(\nu_{\mathcal{L}},e_\lambda). \tag{C.4}$$

The radial inhomogeneity of n_m has no impact on the measurements of M (Sect. 2.4.3) or of the relative density change $v_m = n_m^s(M)/n_m^s(0)$ (Sect. 2.4.4), which rely on the comparison of absorbances sequentially measured with the same laser beam. The absolute measurements of the light transmittance probe the abundance of the 1083 nm absorbers (Sect. 2.4.4) and the average values n_m^s are used to quantitatively characterize the plasma conditions in which MEOP is performed (Sect. 3.1).

C.2 Broadband light absorption measured with a narrow beam

The incident narrow laser beam is here assumed to have a normalized spectral density g_0, distributed around the central frequency $\nu_{\mathcal{L}}$ and characterized by a linewidth $\mathcal{L}$, so that the intensity $\mathcal{I}(0)$ entering the cell is equal to:

$$\mathcal{I}(0) = \mathcal{I}_0\int_0^\infty g_0(\nu)d\nu. \tag{C.5}$$

If $\mathcal{L}$ is comparable to the atomic linewidth (which is the case for the fiber laser used for OP at 4.7 T), for large enough n_m significant differences in attenuation occur for the central part and for the wings of the laser emission spectrum, inducing a change in spectral distribution during propagation. The evolution of the local spectral density of the light, $g(\nu,l)$, is given by:

$$\frac{\partial g}{\partial l} = -n_m(l)\widetilde{\sigma}S(\nu,e_\lambda)g(\nu,l) \tag{C.6}$$

and the equation of propagation for the local intensity $\mathcal{I}(l) = \mathcal{I}_0\int_0^\infty g(\nu,l)d\nu$ is no longer linear:

$$\frac{d\mathcal{I}}{dl} = -n_m(l)\widetilde{\sigma}\int_0^\infty S(\nu,e_\lambda)g(\nu,l)d\nu. \tag{C.7}$$

Spatial integration of equation (C.6) yields:

$$g(\nu,l) = g_0(\nu)\exp\left\{-\widetilde{\sigma}S(\nu,e_\lambda)\int_0^l n_m(l')dl'\right\} \tag{C.8a}$$

$$= g_0(\nu)\exp\left\{\ln\mathcal{T}^*(l)\frac{S(\nu,e_\lambda)}{S(\nu_{\mathcal{L}},e_\lambda)}\right\}, \tag{C.8b}$$

where (for convenience) the path-dependent variation with abscissa l is described by the monochromatic light transmittance $\mathcal{T}^*(l)$ associated with the central frequency $\nu_\mathcal{L}$ obtained in Section C.1 (Eq. (C.2)):

$$\int_0^l n_\mathrm{m}(l')dl' = \frac{-\ln \mathcal{T}^*(l)}{\widetilde{\sigma} S(\nu_\mathcal{L}, e_\lambda)}, \tag{C.9}$$

and

$$\frac{\mathcal{I}(l)}{\mathcal{I}(0)} = \int_0^\infty g_0(\nu) \exp\left\{\ln \mathcal{T}^*(l) \frac{S(\nu, e_\lambda)}{S(\nu_\mathcal{L}, e_\lambda)}\right\} d\nu. \tag{C.10}$$

In the low absorption limit ($-\ln \mathcal{T}^* \simeq 1 - \mathcal{T}^* \ll 1$) a first-order Taylor expansion yields a factorized expression that involves two distinct contributions: the position dependent monochromatic absorptance $(1 - \mathcal{T}^*) \simeq \widetilde{\sigma} S(\nu_\mathcal{L}, e_\lambda) \int_0^l n_\mathrm{m}(l')dl'$ for $\nu = \nu_\mathcal{L}$ and the spectrum dependent integral $\int_0^\infty g_0(\nu)\{S(\nu, e_\lambda)/S(\nu_\mathcal{L}, e_\lambda)\}d\nu$.

Equation (C.10), applied to the particular case $\alpha = 0$, is used in Section C.3 to derive the light transmittance for the attenuated pump beam. It can also be used to compute, for instance, the light absorbance that would be measured in the same set-up if the narrow probe beam were delivered by a broadband laser source. This corresponds to a situation commonly met in practice (e.g., in gas polarizing units) where, for convenience, the light used to probe the plasma is delivered by the monitor output of the broadband fiber laser used for OP, rather than by a dedicated monochromatic laser source. For the V-shaped path depicted in Figure C.1, the broadband light absorbance, $-\ln \mathcal{T}_\mathrm{broad}$, would then be equal to:

$$-\ln \mathcal{T}_\mathrm{broad} = -2 \ln \int_0^\infty g_0(\nu) \exp\left\{\frac{S(\nu, e_\lambda)}{S(\nu_\mathcal{L}, e_\lambda)} \frac{\ln \mathcal{T}_\mathrm{mono}}{2}\right\} d\nu. \tag{C.11}$$

To quantify the impact of the spectral width of the light source, $\mathcal{T}_\mathrm{broad}$ and $\mathcal{T}_\mathrm{mono}$ are numerically compared in Figure C.2 for the case of the fiber laser used for OP at 4.7 T (Gaussian spectral density $g_0(\nu) = (\mathcal{L}\sqrt{\pi})^{-1} \exp\{-(\nu - \nu_\mathcal{L})^2/\mathcal{L}^2\}$, $\mathcal{L} = 1$ GHz). The computations are performed for various atomic linewidths, using Table B.1 FWHM values (Appendix B.2). At $M = 0$, for instance, the departure from $\mathcal{T}_\mathrm{mono}$ is significant and increases linearly with $(1 - \mathcal{T}_\mathrm{broad})$ at low values, as expected (Fig. C.2a). The relative impact of $\mathcal{L}$ is larger for a higher light absorption and for a better match between laser and atomic linewidths (i.e., a smaller 2^3S-2^3P collisional broadening since $\mathcal{L} \approx \tilde{\Delta}_3$). As a consequence, an average value of n_m can no longer be directly inferred from the measured absorbance. Figure C.2b shows that correction factors ranging from 5 to 30% would need to be applied to the average density values erroneously obtained using equation (C.4), valid only for monochromatic light. The non linear link between $-\ln \mathcal{T}_\mathrm{broad}$ and $S(\nu, e_\lambda)$ obtained in equation (C.11) also modifies the way the measured absorbances vary with M. This makes the tools described in Section 2.4.3 inappropriate for accurate polarization measurements. However, an adaptation or modification of these tools may be of little interest if, in practice, the light source used for detection is the broadband laser used for OP. In this case, the Zeeman sublevels probed in the 2^3S state would be addressed also by the pump light and the large OP-induced skew of the populations would need to be quantitatively taken into account (see Appendix C.4).

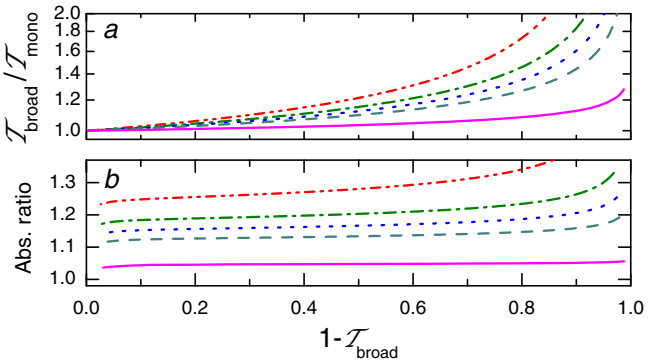

Fig. C.2. Broadband light transmittance $\mathcal{T}_\mathrm{broad}$ expected for a narrow beam with $\mathcal{L} = 1$ GHz Gaussian bandwidth (1.7 GHz FWHM, similar to $\overline{\omega}_\mathrm{G}$). Results are obtained using equation (C.11) and $\mathcal{T}_\mathrm{mono}$ as input variable and referenced to the monochromatic light case (4.7 T, A_2–B_9 line). (a) Transmittance ratio; semi-log plot. (b) Absorbance ratio $-\ln \mathcal{T}_\mathrm{broad}/(-\ln \mathcal{T}_\mathrm{mono})$. From top to bottom: 0.03 (red dash-dot-dot), 0.06 (green dash-dot), 0.09 (blue dot), 0.12 (dark cyan dash), and 0.25 amg (magenta solid).

C.3 Light absorption measured with a non uniform intensity profile

For simplicity the discussion is restricted to the case of absorption measurements performed at 4.7 T with the strongly attenuated pump beam: the incident light has a non uniform transverse profile with radial symmetry and it propagates parallel to the optical axis, passing twice across the gas cell. The transmitted light is collected and the measured power $\mathcal{P}_\mathrm{on}$ or $\mathcal{P}_\mathrm{off}$ (with or without rf excitation, respectively) includes additive contributions from all points of the cell end window, yielding:

$$\frac{\mathcal{P}_\mathrm{on}}{\mathcal{P}_\mathrm{off}} = \frac{\int_0^{R_\mathrm{cell}} \mathcal{I}_\mathrm{on}(\rho) 2\pi\rho d\rho}{\int_0^{R_\mathrm{cell}} \mathcal{I}_\mathrm{off}(\rho) 2\pi\rho d\rho}. \tag{C.12}$$

The intensity attenuation rate $\mathcal{I}_\mathrm{on}(\rho)/\mathcal{I}_\mathrm{off}(\rho)$ depends on the local density $n_\mathrm{m}(\rho)$ and on the laser emission profile:

$$\mathcal{I}_\mathrm{on}(\rho)/\mathcal{I}_\mathrm{off}(\rho) = \exp\{-2L_\mathrm{cell} n_\mathrm{m}(\rho) \widetilde{\sigma} S(\nu_\mathcal{L}, e_\lambda)\} \tag{C.13}$$

for monochromatic light (Eq. (C.4) for $\alpha = 0$) and:

$$\mathcal{I}_\mathrm{on}(\rho)/\mathcal{I}_\mathrm{off}(\rho) = \int_0^\infty g_0(\nu) \exp\{-2L_\mathrm{cell} n_\mathrm{m}(\rho) \widetilde{\sigma} S(\nu, e_\lambda)\} d\nu \tag{C.14}$$

for broadband light (Eq. (C.10)).

In both cases the spatial and spectral contributions can be separated only in the low absorption limit, $1 - \mathcal{T}_{\rm mono}(\rho) \ll 1$ for all ρ. The measured absorbance then still provides limited information on the 2^3S atom density. For monochromatic excitation, a first-order Taylor expansion of equation (C.13) leads to:

$$\frac{\mathcal{P}_{\rm on}}{\mathcal{P}_{\rm off}}(\nu_{\mathcal{L}}, e_\lambda) \simeq 1 - 2L_{\rm cell}\widehat{n_{\rm m}}\widetilde{\sigma}S(\nu_{\mathcal{L}}, e_\lambda). \quad \text{(C.15)}$$

In contrast with $n_{\rm m}^{\rm s}$, $\widehat{n_{\rm m}}$ is a weighted spatial average of $n_{\rm m}$ which depends on the radial light intensity profile:

$$\widehat{n_{\rm m}} = 2\pi \int_0^{R_{\rm cell}} \mathcal{I}_{\rm off}(\rho) n_{\rm m}(\rho) \rho d\rho / \mathcal{P}_{\rm off}. \quad \text{(C.16)}$$

The absorbance $-\ln(\mathcal{P}_{\rm on}/\mathcal{P}_{\rm off})$ then provides less direct information about the density of absorbers. However, it remains proportional to $S(\nu_{\mathcal{L}}, e_\lambda)$ and may be used for measurements of M with the method described in Section 2.4.3. A similar but more complex expression is obtained for broadband excitation:

$$\frac{\mathcal{P}_{\rm on}}{\mathcal{P}_{\rm off}} \simeq (1 - 2L_{\rm cell}\widehat{n_{\rm m}}\widetilde{\sigma}S(\nu_{\mathcal{L}}, e_\lambda)) \times \int_0^\infty g_0(\nu)\{S(\nu, e_\lambda)/S(\nu_{\mathcal{L}}, e_\lambda)\}d\nu \quad \text{(C.17)}$$

and M cannot be directly inferred from transmittance ratios. In MEOP experiments the beam shape and the OP lines are usually chosen so as to maximize pump light absorption. Hence, even at low powers, the intrication of $n_{\rm m}$ and M contributions to the absorbance introduces a prohibitive complexity.

C.4 Light absorption measured during OP

For completeness, it should be emphasized again that the previous derivations rely on the assumption that the cross section σ is uniform. Hence, they are irrelevant for the absorption measurements performed during OP, where the redistribution between the 2^3S sublevels and the promotion from the 2^3S to the 2^3P state both depend on the local OP rate. Even if OP is performed with a uniform light intensity profile and if pump absorption does not vary along the cell axis, the spectral amplitudes depend systematically both on M and on the position inside the cell because $n_{\rm m}$ is not uniform. Numerical computations or exhaustive measurements of the atomic populations are thus needed to derive the light absorbance.

Less effort is sometimes required in MEOP experiments where a few direct measurements can be performed. For instance, the absorbed pump power $W_{\rm abs}$ (hence, the amount of deposited angular momentum) may be measured at arbitrarily high 1083 nm excitation if the discharge can be transiently switched off. In the 4.7 T experiment, the fraction of light power absorbed at $M = 0$ is measured with a strongly attenuated pump beam. However, $1 - \mathcal{T}_{\rm pump}^{\rm att.}$ can only provide an upper bound for $W_{\rm abs}$ during OP since $W_{\rm abs}$ decreases when M increases, because of the ME-enforced approach to spin-temperature distribution in the 2^3S state. $W_{\rm abs}$ also decreases when the OP light power increases, primarily because of the OP-induced skew of the distribution in the 2^3S state (secondarily because of the optical saturation of the transition, i.e., the contribution of stimulated emission to the transmitted ligh power)[19]. The quantitative link between $\mathcal{T}_{\rm pump}^{\rm att.}$ and the pump transmittance $\mathcal{T}_{\rm pump}$ at full power and finite polarization M must then be numerically investigated using a reliable MEOP model, in order to compute $W_{\rm abs}$ (see figures 5 and 6 in Ref. [24], for instance).

Computation of the impact of OP light on the probe transmittance is also needed and challenging for accurate measurements of M or $n_{\rm m}$. In practice, thanks to the very short optical time scales, for the polarization measurements a direct comparison of absorption data obtained with and without OP light can be pragmatically performed at fixed plasma conditions and gas density. This is cumbersome but manageable and high reliability has been demonstrated at low field [14,24]. Fortunately no such effort is needed at high field (thanks to hyperfine decoupling) for an appropriate choice of the probe lines (see Sect. 2.4.3).

In conclusion, optical detection based on 1083 nm light absorption is a sensitive and versatile technique that must be carefully implemented to provide accurate measurements of M and $n_{\rm m}$.

Appendix D: Correction functions

At low and moderate gas density M and $v_{\rm m}$ are straightforwardly obtained as $M = M^{\rm raw}$ and $v_{\rm m} = v_{\rm m}^{\rm raw}$ (Eqs. (12) and (17)). At high density they are inferred from $M^{\rm raw}$ and $v_{\rm m}^{\rm raw}$ using the correction functions $\delta M^{\rm corr}$ (Eq. (14)) and $v_{\rm m}^{\rm corr}$ (Eq. (18)), computed once for each cell. Using the best-fit FWHM values of Table B.1, S^+ is computed for a periodic series of frequencies (varying linearly up and down between the experimental scan boundaries), for $M = 0$ during the first two periods then for M varying linearly from 0 to -1. The ensemble of computed probe doublet spectra is processed exactly as an experimental one[20]. This yields a set of average time abscissas t_n and output values $q_i'(t_n)$, $r_{21}(t_n)$, and $M^{\rm raw}(t_n)$ for which the true polarization is known and equal to the input value $M = M(t_n)$. The quantities $\delta M^{\rm corr}(t_n)$ and $v_{\rm m}^{\rm corr}(t_n)$ are then computed and polynomial fits are performed to obtain analytical correction functions.

[19] At low pressure the loss of OP beam efficiency due to saturation can be minimized by the use of a broadband laser source with a spectral density distribution matched to the Doppler-broadened atomic line profile, which is optimally suited for simultaneous excitation of all velocity classes [39].

[20] In practice, the spectra are processed from $M = 0$ to some end value where the two lines coalesce and the peak heights cannot be simply picked. A more detailed analysis of the features of the spectra would need to be performed for higher M.

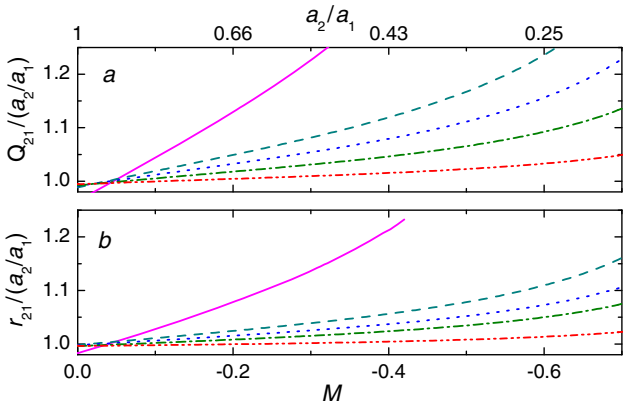

Fig. D.1. Computed variations of the peak amplitude ratios Q_{21} (a) (no correction) and r_{21} (b) (with baseline correction), scaled to the population ratio a_2/a_1 (spin-temperature equilibrium, 4.7 T). Density decreases from top to bottom (N_0 values, line styles and colors: see Fig. C.2).

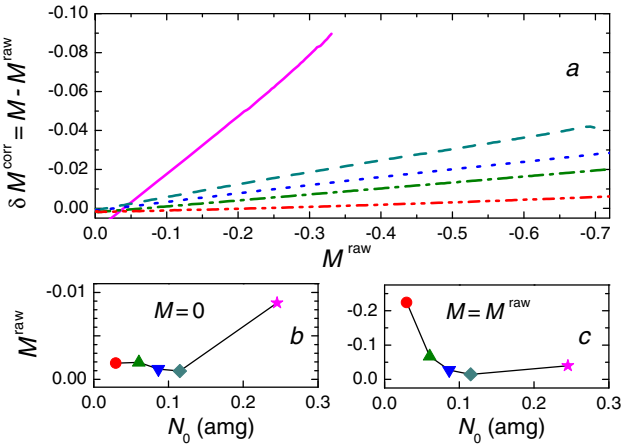

Fig. D.2. Impact of line broadening on the discrepancy between M and $M^{\rm raw}$ at 4.7 T. (a) Variation of $\delta M^{\rm corr}$ with $M^{\rm raw}$. Density decreases from top to bottom (N_0 values, line styles and colors: see Fig. C.2). (b) Values of $M^{\rm raw}$ obtained at $M = 0$ (noted $M_0^{\rm raw}$ in the text). (c) Values of $M^{\rm raw}$ for which $\delta M^{\rm corr} = 0$.

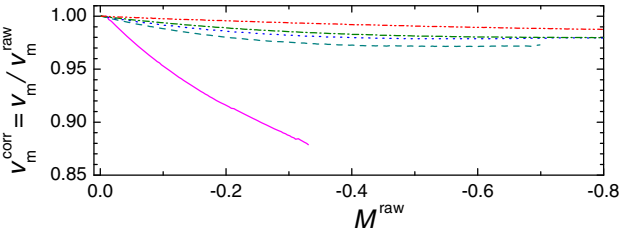

Fig. D.3. Impact of line broadening on the correction factor $v_{\rm m}^{\rm corr}$ at 4.7 T (A_2-B_9 line). Density increases from top to bottom (N_0 values, line styles and colors: see Fig. C.2).

The major advantage of this correction method is that it only involves the baseline-corrected peak amplitudes q_i', whose ratios are more robust against experimental imperfections (such as residual offsets in the recorded signals) than the genuine peak values q_i. Another advantage is that, as shown below, the corrections required at 4.7 T are small for $N_0 \leq 0.09$ amg and vary almost linearly with M up to 0.25 amg. A good accuracy is therefore obtained with a 1st or 2nd order polynomial adjustment. The results are presented in Appendices D.1 and D.2. The application to polarization measurements performed at other field strengths is briefly discussed in Appendix D.3.

D.1 Polarization measurements at high gas density

Figure D.1 shows the evolution of the discrepancy between the peak amplitude ratio and the population ratio a_2/a_1 with gas polarization and density. Comparison is made for the results obtained with the reduced ratio used for M measurements, $r_{21} = q_2' T_{1,10}/q_1' T_{2,9}$ (Fig. D.1b), and with a similar ratio computed from the genuine peak amplitudes, $Q_{21} = q_2 T_{1,10}/q_1 T_{2,9}$ (Fig. D.1a). The baseline correction leads to significantly smaller deviations for densities up to 0.12 amg (less than 10% for $-0.6 \leq M \leq 0$). The deviation remains notably large for $N_0 = 0.25$ amg, due to the strong overlap of the two probe lines. The impact of these deviations on the quantitative difference between M and $M^{\rm raw}$ is shown in Figure D.2. At fixed $M^{\rm raw}$, $\delta M^{\rm corr}$ increases when the atomic linewidth increases (Fig. D.2a). The values $M^{\rm raw}$ obtained at $M = 0$ are all negative ($M_0^{\rm raw}$, Fig. D.2b). These small finite values are due to residual differences between the adjusted and the true slanted baselines. They are of the order of the experimental error bars. Figure D.2c shows that the points where $M^{\rm raw}$ and M are equal ($\delta M^{\rm corr} = 0$ in Fig. D.2a) lie at low nuclear polarizations (a few percents, except for $N_0 = 0.03$ amg).

The baseline correction provides a value of $M^{\rm raw}$ that is fairly close to the true polarization at moderate density, with a relative underestimation of $|M|$ not exceeding 0.7% (resp. 2.7%) at 0.03 (resp. 0.06) amg for $M \simeq -0.6$ (largest value achieved with the f_2^- OP line). This is in salient contrast with the results obtained at 0.25 amg where OP yields $M \simeq -0.26$ and $\delta M^{\rm corr}/M$ reaches 20%. Overlooking the polarization dependent departure of $M^{\rm raw}$ from M would thus lead to significant systematic errors in the measurements of MEOP dynamics.

D.2 2^3S atom density measurements at high gas density

The results obtained for $v_{\rm m}^{\rm corr}$ with the same series of computed spectra are displayed in Figure D.3. The correction factors are very small for $N_0 \leq 0.12$ amg. At 0.25 amg $v_{\rm m}^{\rm raw}$ overestimates $v_{\rm m}$ by more than 10% at $M = -0.4$.

D.3 Accurate measurements at other field strengths

The numerical data displayed in Figures D.2 and D.3 are obtained at $B = 4.7$ T for the operating conditions and scan boundaries of the experiment. Even if the latter could be reproduced at weaker or stronger B, the correction functions required for accurate M and $n_{\rm m}$ measurements would be different because the 2^3S-2^3P hfs is

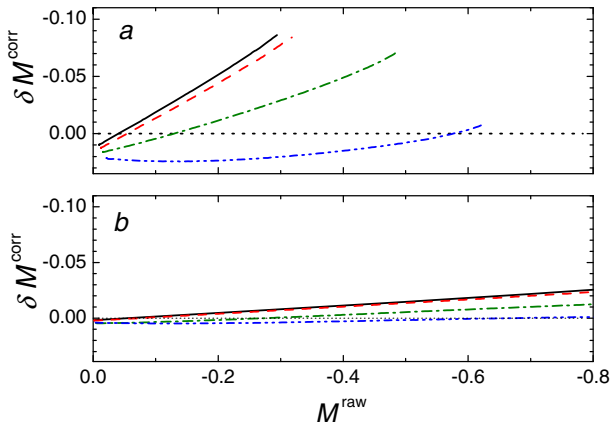

Fig. D.4. Variation of $\delta M^{\rm corr}$ with the field strength at high and moderate density ((a) 0.25 amg, (b) 0.06 amg; computation with scan boundaries and FWHM values at 4.7 T). $B = 7$ (black solid), 4.7 (red dash), 2 (green dash-dot), and 1.5 T (blue dash-dot-dot). Dotted line: $M = M^{\rm raw}$.

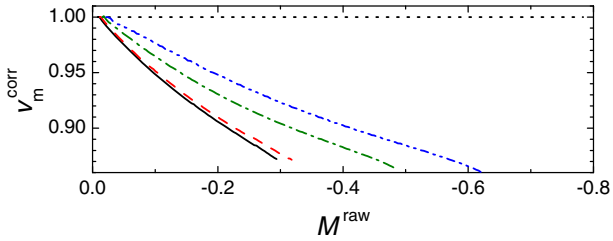

Fig. D.5. Variation of $v_{\rm m}^{\rm corr}$ with B at high gas density (0.25 amg, A_2-B_9 line; same legend and computations as in Fig. D.4).

not the same. This is shown in Figure D.4 for $\delta M^{\rm corr}$ and gas densities $N_0 = 0.06$ and 0.25 amg, in the 1.5–7 T range[21]. As expected, fairly similar differences between M and $M^{\rm raw}$ are obtained at 4.7 and 7 T because the (hyperfine) Zeeman splitting between the two probe lines weakly varies with B, while the (fine) splittings between the line doublet and the other σ^+ lines strongly increase. The correction $\delta M^{\rm corr}$ is significantly smaller at $B = 2$ T than at 4.7 T, over a broad range of polarization. Finally $\delta M^{\rm corr}$ is found to be notably small at $B = 1.5$ T, not exceeding +0.5% at 0.06 amg and −2.5% at 0.25 amg in the $-0.6 \leq M \leq 0$ range, thanks to the different combinations of Zeeman shifts and transition matrix elements obtained for this field strength.

A similar comparison indicates that, over the same M range, $v_{\rm m}^{\rm raw}$ leads to a small overestimation of $v_{\rm m}$ at low density (by less than 3% for $N_0 = 0.06$ amg, data not shown) and that the difference between the two values decreases monotonically when B increases at high density (Fig. D.5). In contrast with $\delta M^{\rm corr}$, the correction $v_{\rm m}^{\rm corr}$ remains significant at all field strengths. Unsurprisingly, B has a different impact on the individual values and on the ratio of the probe line peak heights.

[21] A different detection scheme must be used at 0.9 T (another line lies between the two probe ones) and at 0.45 T for high N_0 (the probe lines are no longer separated from the f_2^+ line).

References

1. F.D. Colegrove, L.D. Schearer, G.K. Walters, Phys. Rev. **132**, 2561 (1963)
2. P.-J. Nacher, M. Leduc, J. Phys. **46**, 2057 (1985)
3. M. Leduc, P.-J. Nacher, G. Tastevin, E. Courtade, Hyperf. Interact. **127**, 443 (2000)
4. P.-J. Nacher, E. Courtade, M. Abboud, A. Sinatra, G. Tastevin, T. Dohnalik, Acta Phys. Polon. B **33**, 2225 (2002)
5. M. Abboud, A. Sinatra, X. Maitre, G. Tastevin, P.-J. Nacher, Europhys. Lett. **68**, 480 (2004)
6. J. Becker, W. Heil, B. Krug, M. Leduc, M. Meyerhoff, P.-J. Nacher, E. Otten, T. Prokscha, L. Schearer, R. Surkau, Nucl. Instrum. Methods Phys. Res. A **346**, 45 (1994)
7. P.-J. Nacher, G. Tastevin, X. Maitre, X. Dollat, B. Lemaire, J. Olejnik, Eur. Radiol. **9**, B18 (1999)
8. T. Gentile et al., Magn. Res. Med. **43**, 290 (2000)
9. L. Darrasse, G. Guillot, P.-J. Nacher, G. Tastevin, C. R. Acad. Sci. Paris Série IIb **324**, 691 (1997)
10. E. Courtade, Ph.D. thesis, Université Pierre et Marie Curie, Paris, France, 2001, http://tel.archives-ouvertes.fr/tel-00001447
11. E. Courtade, F. Marion, P.-J. Nacher, G. Tastevin, T. Dohnalik, K. Kiersnowski, Hyperf. Interact. **127**, 451 (2000)
12. J.L. Flowers, B.W. Petley, M.G. Richards, J. Phys. B **23**, 1359 (1990)
13. A. Nikiel, T. Palasz, M. Suchanek, M. Abboud, A. Sinatra, Z. Olejniczak, T. Dohnalik, G. Tastevin, P.-J. Nacher, Eur. Phys. J. Special Topics **144**, 255 (2007)
14. M. Batz, Ph.D. thesis, UPMC - Paris 6, France and J. Gutenberg Universität, Mainz, Germany, 2011, http://tel.archives-ouvertes.fr/tel-00665393
15. E. Courtade, F. Marion, P.-J. Nacher, G. Tastevin, K. Kiersnowski, T. Dohnalik, Eur. Phys. J. D **21**, 25 (2002)
16. M. Abboud, Ph.D. thesis, Université Pierre et Marie Curie, Paris, France, 2005, http://tel.archives-ouvertes.fr/tel-00011099/
17. T. Dohnalik, A. Nikiel, T. Palasz, M. Suchanek, G. Collier, M. Grenczuk, B. Glowacz, Z. Olejniczak, Eur. Phys. J. Appl. Phys. **54**, 20802 (2011)
18. K. Suchanek, M. Suchanek, A. Nikiel, T. Palasz, M. Abboud, A. Sinatra, P.-J. Nacher, G. Tastevin, Z. Olejniczak, T. Dohnalik, Eur. Phys. J. Special Topics **144**, 67 (2007)
19. C. Talbot, M. Batz, P.-J. Nacher, G. Tastevin, J. Phys.: Conf. Ser. **294**, 012008 (2011)
20. A. Nikiel, Ph.D. thesis, Jagiellonian University, Krakow, Poland, 2011
21. W.A. Fitzsimmons, N.F. Lane, G.K. Walters, Phys. Rev. **174**, 193 (1968)
22. R. Deloche, P. Monchicourt, M. Cheret, F. Lambert, Phys. Rev. A **13**, 1140 (1976)
23. M. Abboud, A. Sinatra, G. Tastevin, P.-J. Nacher, X. Maitre, Laser Phys. **15**, 475 (2005)
24. M. Batz, P.-J. Nacher, G. Tastevin, J. Phys.: Conf. Ser. **294**, 012002 (2011)
25. *Handbook of atomic, molecular, and optical physics*, edited by G. Drake (Springer, 2006), Chap. 11.5
26. D. Bloch, G. Trenec, M. Leduc, J. Phys. B **18**, 1093 (1985)
27. K. Tachibana, Y. Kishimoto, O. Sakai, J. Appl. Phys. **97**, 123301 (2005)

28. T. Zelevinsky, Ph.D. thesis, Harvard University, Cambridge, USA, 2004
29. D. Vrinceanu, S. Kotochigova, H.R. Sadeghpour, Phys. Rev. A **69**, 022714 (2004)
30. R. Barbé, M. Leduc, F. Laloë, J. Phys. **35**, 935 (1974)
31. N.P. Bigelow, P.-J. Nacher, M. Leduc, J. Phys. II **2**, 2159 (1992)
32. T.R. Gentile, R.D. McKeown, Phys. Rev. A **47**, 456 (1993)
33. M. Batz, S. Baessler, W. Heil, E. Otten, D. Rudersdorf, J. Schmiedeskamp, Y. Sobolev, M. Wolf, J. Res. Natl. Inst. Stand. Technol. **110**, 293 (2005)
34. G. Collier, Ph.D. thesis, Jagiellonian University, Krakow, Poland, 2011, http://www4.fais.uj.edu.pl/pracedr/Guilhem_Collier_2011.pdf
35. E. Stoltz, M. Meyerhoff, N. Bigelow, M. Leduc, P.-J. Nacher, G. Tastevin, Appl. Phys. B: Lasers Opt. **63**, 629 (1996)
36. C. Larat, Ph.D. thesis, Université Pierre et Marie Curie, Paris, France, 1991, http://tel.archives-ouvertes.fr/tel-00011879
37. G. Collier, T. Palasz, A. Wojna, B. Glowacz, M. Suchanek, Z. Olejniczak, T. Dohnalik, J. Appl. Phys. **113**, 204905 (2013)
38. W.H. Press, S.A. Teukolsky, W.T. Vetterling, B.P. Flannery, in *Numerical Recipes: The Art of Scientific Computing*, 3rd edn. (Cambridge University Press, Cambridge, 2007), Chap. 10
39. G. Tastevin, S. Grot, E. Courtade, S. Bordais, P.-J. Nacher, Appl. Phys. B: Lasers Opt. **78**, 145 (2004)